# JGR Oceans

**Key Points:**

- Release and mixing of glacial freshwater drives distinct seasonal circulation styles that control heat transport
- Summer circulation draws warm surface water to the glacier grounding line, yet sill-driven mixing cools the inflow
- Majority of glacial freshwater is refluxed at the entrance sill, regulating near-glacier water properties

**Correspondence to:**

A. O. Hager,
ahager@uoregon.edu

**Author Contributions:**

**Conceptualization:** Alexander O. Hager, David A. Sutherland
**Data curation:** Alexander O. Hager, David A. Sutherland, Jason M. Amundson, Rebecca H. Jackson, Christian Kienholz, Roman J. Motyka, Jonathan D. Nash
**Formal analysis:** Alexander O. Hager, Christian Kienholz
**Funding acquisition:** David A. Sutherland, Jason M. Amundson, Roman J. Motyka, Jonathan D. Nash
**Investigation:** Alexander O. Hager
**Methodology:** Alexander O. Hager, Christian Kienholz
**Project Administration:** David A. Sutherland, Jason M. Amundson, Rebecca H. Jackson, Roman J. Motyka, Jonathan D. Nash

# Subglacial Discharge Reflux and Buoyancy Forcing Drive Seasonality in a Silled Glacial Fjord

Alexander O. Hager[1] , David A. Sutherland[1] , Jason M. Amundson[2] ,
Rebecca H. Jackson[3] , Christian Kienholz[2], Roman J. Motyka[2,4], and Jonathan D. Nash[5]

[1]Department of Earth Sciences, University of Oregon, Eugene, OR, USA, [2]Department of Natural Sciences, University of Alaska Southeast, Juneau, AK, USA, [3]Department of Marine and Coastal Sciences, Rutgers University, New Brunswick, NJ, USA, [4]Geophysical Institute, University of Alaska Fairbanks, Fairbanks, AK, USA, [5]College of Earth, Ocean, and Atmospheric Sciences, Oregon State University, Corvallis, OR, USA

**Abstract** Fjords are conduits for heat and mass exchange between tidewater glaciers and the coastal ocean, and thus regulate near-glacier water properties and submarine melting of glaciers. Entrainment into subglacial discharge plumes is a primary driver of seasonal glacial fjord circulation; however, outflowing plumes may continue to influence circulation after reaching neutral buoyancy through the sill-driven mixing and recycling, or reflux, of glacial freshwater. Despite its importance in non-glacial fjords, no framework exists for how freshwater reflux may affect circulation in glacial fjords, where strong buoyancy forcing is also present. Here, we pair a suite of hydrographic observations measured throughout 2016–2017 in LeConte Bay, Alaska, with a three-dimensional numerical model of the fjord to quantify sill-driven reflux of glacial freshwater, and determine its influence on glacial fjord circulation. When paired with subglacial discharge plume-driven buoyancy forcing, sill-generated mixing drives distinct seasonal circulation regimes that differ greatly in their ability to transport heat to the glacier terminus. During the summer, 53%–72% of the surface outflow is refluxed at the fjord's shallow entrance sill and is subsequently re-entrained into the subglacial discharge plume at the fjord head. As a result, near-terminus water properties are heavily influenced by mixing at the entrance sill, and circulation is altered to draw warm, modified external surface water to the glacier grounding line at 200 m depth. This circulatory cell does not exist in the winter when freshwater reflux is minimal. Similar seasonal behavior may exist at other glacial fjords throughout Southeast Alaska, Patagonia, Greenland, and elsewhere.

**Plain Language Summary** Where glaciers flow directly into oceans, fjords transport heat from the open ocean to glacier fronts. Conversely, fjords are also responsible for exporting meltwater from glaciers to the coast. However, the mixing of warm ocean water and outflowing meltwater can have important implications for fjord circulation, and thus the temperature of water that reaches the glacier front. Here, we pair observations of water temperature, salinity, and velocity measured throughout 2016–2017 in LeConte Bay, Alaska, with computer model experiments to demonstrate that the release and subsequent heavy mixing of glacial meltwater drives pronounced seasonal changes in the circulation of the fjord that affect the transport of heat to the glacier front. We expect similar processes may be taking place in fjords throughout Southeast Alaska and Patagonia, as well as certain fjords in Greenland.

## 1. Introduction

Ocean-induced frontal ablation is a dominant driver of ice dynamics and mass loss for tidewater glaciers (Joughin et al., 2012; McNabb et al., 2015; Nick et al., 2009; Smith et al., 2020), and thus sea level rise in the 21st century (Dieng et al., 2017; Gardner et al., 2013). Glacier retreat and acceleration have been observed following warming ocean temperatures (e.g., Holland et al., 2008; Luckman et al., 2015; Motyka et al., 2011; Murray et al., 2010; Straneo & Heimbach, 2013; Wood et al., 2018), yet fjords often regulate the degree of ocean forcing these glaciers experience (Straneo & Cenedese, 2015), as well as the export of glacial freshwater to the coastal ocean (Bamber et al., 2018, 2012). Near-glacier water properties depend on fjord circulation, which may vary with changes in subglacial discharge (Carroll et al., 2015; Jackson & Straneo, 2016; Sciascia et al., 2013; Straneo et al., 2011; Xu et al., 2012), glacier and iceberg submarine melting (Davison et al., 2020; Jackson et al., 2020; Magorrian & Wells, 2016; Moon et al., 2018), wind forcing (Jackson & Straneo, 2016; Jackson et al., 2014; Moffat, 2014; Moffat et al., 2018), fjord-shelf density gradients (Carroll et al., 2018; Mortensen et al., 2011),

**Resources:** David A. Sutherland, Roman J. Motyka, Jonathan D. Nash
**Supervision:** David A. Sutherland, Jason M. Amundson, Rebecca H. Jackson, Roman J. Motyka, Jonathan D. Nash
**Validation:** Alexander O. Hager
**Visualization:** Alexander O. Hager
**Writing – original draft:** Alexander O. Hager
**Writing – review & editing:** Alexander O. Hager, David A. Sutherland, Jason M. Amundson, Rebecca H. Jackson, Christian Kienholz, Roman J. Motyka

and hydraulic control over sills (Schaffer et al., 2020). In this article, we quantify an additional control on glacial fjord circulation, the sill-driven mixing and recycling of glacial freshwater, and determine its influence on the seasonal variability of fjord circulation and near-glacier water properties when paired with the buoyancy forcing of subglacial discharge plumes.

Fjords are deep estuaries that are often highly stratified (Geyer & Ralston, 2011). Vertical mixing is mostly localized at bathymetric sills (Ebbesmeyer & Barnes, 1980), or in the case of glacial fjords, within subglacial discharge plumes (Carroll et al., 2015; Jenkins, 2011). Ambient near-glacier water properties are therefore largely determined through the volumes and compositions of inflowing external water, outflowing glacially modified water, and the degree of sill-driven mixing that occurs between the two. In addition to external forcing mechanisms, sill-driven mixing may also affect the timing and magnitude of deep water (below sill depth) renewal events (e.g., Farmer & Freeland, 1983; Gade & Edwards, 1980; Geyer & Cannon, 1982; Gillibrand et al., 1995), and thus often the advection of external water to the glacier grounding line. For example, sill-driven reflux (the vertical mixing and recirculation) of freshwater may sufficiently freshen inflow so to prevent deep water renewal (Geyer & Cannon, 1982; Gillibrand et al., 1995), or if mixing persists long enough, may freshen ambient fjord conditions to facilitate more frequent renewal events (Gillibrand et al., 1995).

Subglacial discharge buoyancy forcing has recently been identified as an important mechanism for deep water renewal in glacial fjords (e.g., Carroll et al., 2017; Gladish et al., 2015; Zhao et al., 2021). Yet, the strong seasonality of glacial freshwater fluxes (Bamber et al., 2018; Jackson & Straneo, 2016; Moon et al., 2018) implies this renewal mechanism is only active for part of the year. Freshwater reflux is similarly seasonal, and it should be expected that both subglacial discharge reflux and buoyancy forcing drive large changes in stratification, circulation, and heat advection between seasons. However, due to the inaccessibility of many glacial fjords in the winter, few year-round studies have observed the seasonal evolution of silled glacial fjord circulation (e.g., Matthews, 1981; Moffat et al., 2018; Mortensen et al., 2014), and it remains unclear how subglacial discharge and reflux affect heat advection to tidewater glacier termini throughout the year.

Here, we use a suite of observations collected throughout 2016–2017 in LeConte Bay, Alaska, to investigate the seasonal relationship between sill-generated mixing and plume-driven buoyancy forcing in a shallow-silled glacial fjord. We complement our observations with experiments using the Massachusetts Institute of Technology general circulation model (MITgcm; Marshall et al., 1997), and employ the estuarine Total Exchange Flow (TEF) framework (MacCready, 2011) to calculate reflux fraction at bathymetric sills (Cokelet & Stewart, 1985; MacCready et al., 2021). We find a majority of glacial freshwater is refluxed at the fjord's shallow entrance sill, which when paired with a deep buoyancy source at the glacier terminus, creates a distinct summer circulation regime only feasible in silled, glacial fjords. In the summer, this circulatory cell has two competing effects on heat advection: (a) warm and relatively salty externally surface water is rapidly drawn down a series of sills to the 200 m deep grounding line; however, (b) this inflowing water also undergoes heavy sill-driven mixing with the outflowing plume, thereby cooling substantially upon entering the fjord. We anticipate our results are directly applicable to other shallow-silled glacial fjords throughout Alaska, Canada, and Patagonia, as well as in some fjords in Greenland with the proper geometric constraints.

## 2. Methods

### 2.1. Study Area: LeConte Bay, Alaska

LeConte Bay is a 25 km long, 1–2 km wide glacial fjord in Southeast Alaska (Figure 1). The fjord contains a series of four sills and sub-basins along its length. At the fjord mouth is a 4 km long, 8–20 m deep, sill (S1) that modulates exchange flow between LeConte Bay and Frederick Sound (Motyka et al., 2013). Exchange flow across S1 is aided by strong tidal forcing, with mixed semi-diurnal tidal amplitudes ranging between 2.5 and >6 m (O'Neel et al., 2001). Three more sills (S2, S3, and S4) exist at 12, 1.7 km, and <500 m from the LeConte Glacier terminus, with maximum depths of ~90, ~180, and ~170 m, respectively. Sub-basins (B1–B4) reside between sills, and range in depths from ~135 to ~320 m (Figure 1c). During our study period, the depth of the glacier grounding line was ~200 m, deeper than any of the four sills. A subglacial discharge plume was observed near the southern extent of the glacier terminus throughout both summers of 2016–2017 (Kienholz et al., 2019; Sutherland et al., 2019a); however, plumes have occasionally been observed near the northern terminus in other years (Motyka et al., 2013).
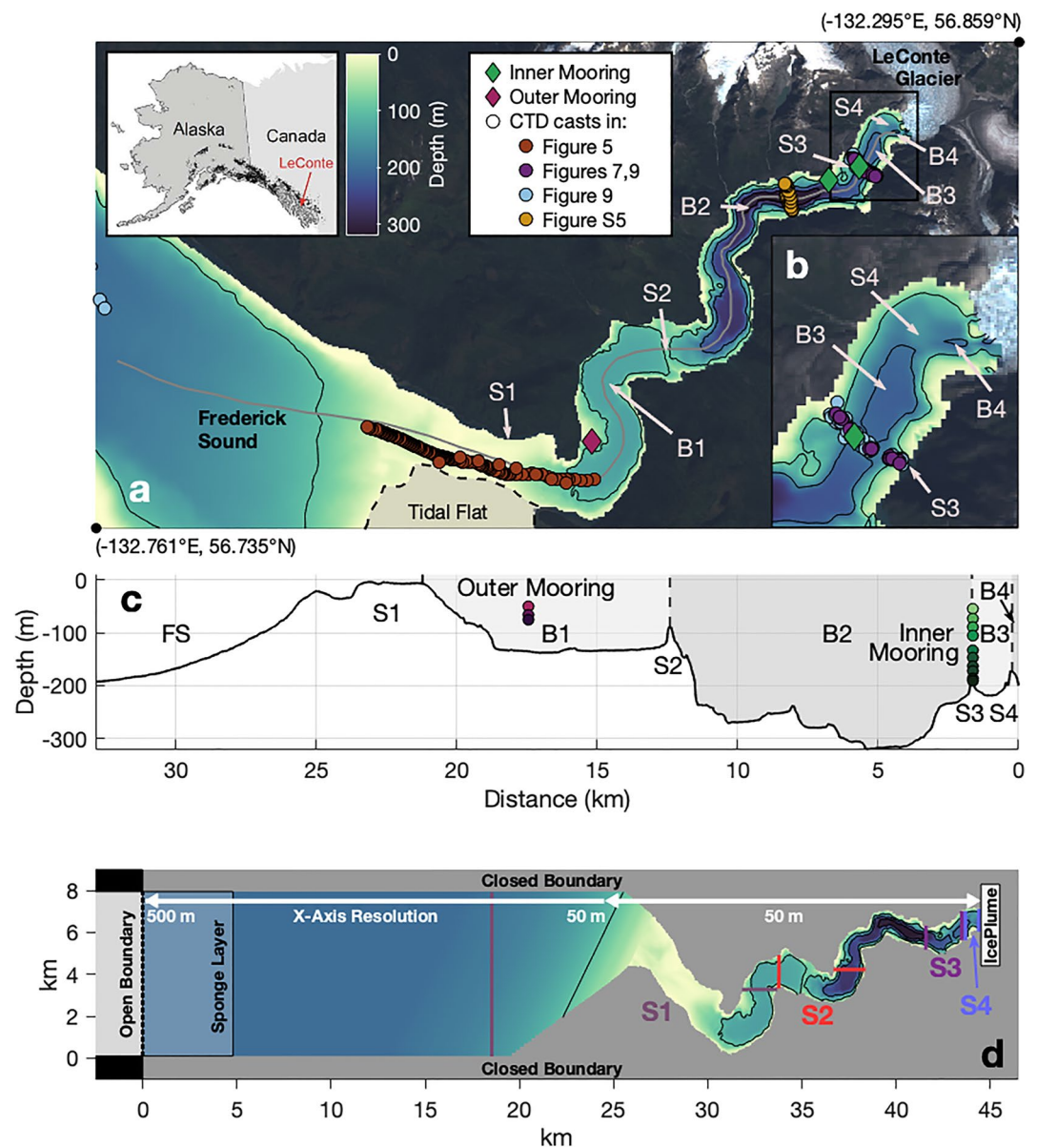
**Figure 1.** (a) Bathymetric map of LeConte Bay, including the locations of sills, sub-basins, moorings (including both Inner Mooring locations), and shipboard CTD casts from subsequent figures. (b) Zoom-in of the black box in (a). (c) Thalweg bathymetry along gray line in (a), including sills, sub-basins, and locations of all mooring instruments. Instrument colors coincide with Figure 3. (d) MITgcm model domain including the locations of the TEF efflux/reflux transects bracketing each sill. Contours in (a, b) and (d) are at 100 m intervals.

## 2.2. Shipboard Data Collection and Processing

Shipboard observations consist of hydrographic and water velocity data from six field surveys during March/April 2016–September 2017. We conducted three extensive shipboard surveys in August 2016, May 2017, and September 2017 with instrumentation on two separate vessels, the MV Pelican and MV Steller, sampling concurrently. Three additional surveys in March/April 2016, October 2016, and July 2017 used only the MV Pelican. Shipboard temperature, salinity, and pressure data were collected using a vertical microstructure profiler (VMP; Rockland Scientific VMP-500) and conductivity, temperature, and pressure profilers (CTDs; Seabird 19plus and RBRconcerto), and were vertically averaged into 1 m bins. CTDs and the VMP were cross-calibrated at the beginning of each survey period. Two acoustic Doppler Current Profilers (ADCPs; 600 and 150 kHz Teledyne Workhorse) were mounted on the MV Pelican, and a 300 kHz ADCP (Teledyne Workhorse) was mounted on the

MV Steller. All ADCPs were operating continuously during CTD sampling to obtain concurrent hydrography and velocity profiles. The 600, 300, and 150 kHz ADCP data were vertically averaged into 2, 5, and 6 m bins, respectively, and horizontally averaged into 30 m bins. We removed data within the bottom 15% of the water column, and within 4 m, 5 m, and 10 m of the surface for the 600, 300, and 150 kHz ADCPs, respectively. We also set an autocorrelation threshold for each beam, and removed all data with a signal-to-noise ratio of less than 110 (out of 128). Binned data from consecutive pairs of across-fjord ADCP transects were averaged together to improve their reliability.

### 2.3. Mooring Data Collection and Processing

Two moorings were deployed in LeConte Bay during our study period. The Inner Mooring contained 11 temperature, salinity, and/or pressure sensors (RBRsoloD, RBRsoloT, RBRduo, Seabird SBE56, Seabird SBE37 Micro-CAT) between 58–200 m depth (Figure 1b). Iceberg coverage precluded any shallower instrumentation. We stationed the Inner Mooring 2.8 km from the glacier terminus between March and August 2016, then relocated it to 1.9 km from the terminus until September 2017 (Figure 1a). The Outer Mooring was located 18 km from the glacier terminus between August 2016 and September 2017, and was equipped with four temperature, salinity, and/or pressure instruments (Onset HOBO PT, RBRsoloT, Seabird SBE37 MicroCAT) between 47 and 78 m depth (Figure 1). Hydrographic instruments on all moorings sampled at 1 s to 30 min intervals, and the data was later interpolated to 15 min. Short gaps exist in all mooring data in August 2016 and May 2017 when the instruments were retrieved for servicing. Salinity time series were filtered to remove significant outliers (five standard deviations from a moving mean). Additional data gaps resulted from instruments losing power or behaving erratically.

### 2.4. Modeled Subglacial Discharge

Glacial runoff during our study period was modeled using an enhanced temperature index model (Hock, 1999), coupled with an accumulation model and linear reservoir-based discharge routing model (Hock & Noetzli, 1997). Modeled runoff is a product of all glacial meltwater and liquid precipitation in the glacier watershed. To account for poorly constrained parameters, we generated high, medium, and low run-off scenarios, where the medium scenario used a parameter combination that minimizes the root mean square error between modeled and observed specific mass balance measurements. The model was previously published in Amundson et al. (2020) and Sutherland et al. (2019a), which include further details of its implementation.

### 2.5. MITgcm Setup and Experiments

We used the Massachusetts Institute of Technology general circulation model (MITgcm; Marshall et al., 1997) to calculate the reflux of plume water at each sill, and to fill observational gaps needed for hypothesis testing. Experiments were designed to resemble either winter or summer fjord conditions, and were forced with either spring or neap tides, along with a range of subglacial discharge rates typical of each season.

Model bathymetry was constructed using data from a 5 m resolution multibeam echosounder (Reson SeaBat 7111) survey in August 2016, with data gaps filled in using two 20 m resolution fathometer (Furuno 528L) surveys in August 1999 and September 2000 (Eidam et al., 2020). Observed fjord bathymetry was then interpolated onto the $50 \times 50$ m model grid (Figure 1d). Outside of S1, we constructed an artificial 25 km extension to the domain with similar depth (200 m) and width (8 km) as Frederick Sound. Resolution in the x-direction of the extended domain telescopes from 50 m at S1 to 500 m at the open boundary on the western extent. A sponge layer 10 grid cells (4.8 km) thick existed along the open boundary to mitigate reflection of internal waves back into the domain. Fjord bathymetry was rotated 49° clockwise to best fit onto a rectangular grid and minimize the number of dry cells. Vertical resolution of our model was 2.5 m in the upper 20 m, 5 m at 20–90 m depth, 10 m at 90–200 m depth, and 25 m at 200–325 m depth.

Idealized tides were implemented by imposing an oscillating tidal velocity along the open boundary, and were tuned so that the amplitudes of tidal pressure variations resemble those observed at the Inner and Outer Moorings. Experiments were forced with symmetric semidiurnal tides with a constant amplitude of 5.5 or 2.8 m to reflect
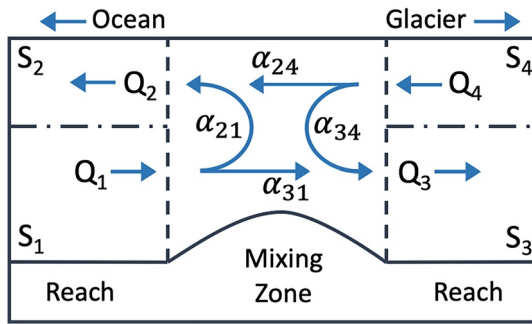
**Figure 2.** Schematic illustrating the different variables in efflux/reflux theory across a sill-generated mixing zone.

typical spring or neap tides, respectively. We used shipboard $\theta/S$ profiles from March/April and August 2016 to initialize our winter and summer experiments, respectively.

We grouped $\theta/S$ profiles measured into six regions: Frederick Sound, S1, B1, B2, B3, and B4, then initialized our model with the observed maximum and mean $\theta$ and $S$ profiles, respectively, in each (Figure S1 in Supporting Information S1). Any resultant $\theta/S$ gradients between regions were smoothed during the spin-up process. For each season, we spun-up the model with neap tidal forcing until reaching steady state (defined as the point when TEF salt fluxes converge to constant values), then restarted with either neap or spring tides, and ran the model until it re-equilibrated to a quasi-steady state. A quasi-steady state was typically reached within 20 or 30 days of model time for summer and winter runs, respectively.

Subglacial discharge and submarine melt were parameterized using the IcePlume Package (Cowton et al., 2015) using a straight glacier terminus on the eastern extent of our domain (Figure 1d). We forced the model with a subglacial discharge plume at 200 m depth on the south side of the terminus, which is consistent with multibeam sonar surveys (Sutherland et al., 2019a) and time-lapse photography (Kienholz et al., 2019) conducted during our study period. For summer experiments, neap and spring tide scenarios were each run with constant subglacial discharge forcing of either 150, 250, or 350 m$^3$ s$^{-1}$ (Table S1 in Supporting Information S1). We neglected subglacial discharge in the winter formulation. We used a line-plume parameterization (Jenkins, 2011) considering a channel width of 100 m, which was based on estimates of plume geometry and discharge during our August 2016 survey (e.g., Jackson et al., 2017). Individual line-plume length is limited by horizontal grid resolution (50 m), so the 100 m long line-plume consists of two adjacent 50 m line-plumes, with the total discharge split evenly between the two. This approach generates the desired entrainment rate of a 100 m line-plume, although interaction between the plumes may make flow nearest to the terminus unrealistic. A small ($\sim 10^{-4}$) negative velocity was evenly imposed across the open boundary to compensate for the volume of water entering the domain. We tuned the IcePlume background water velocity to 0.9 m s$^{-1}$ for our summer experiments to increase ambient submarine melting so that the area-averaged melt rate resembled the observed rate of 8–8.5 m d$^{-1}$ (Jackson et al., 2020; Sutherland et al., 2019a). This was necessary because standard theory significantly underpredicts ambient submarine melting at LeConte Glacier (Jackson et al., 2020). Part of the discrepancy between theory and observations is caused by plume-driven horizontal circulation along the ice face (Jackson et al., 2020; Slater et al., 2018), so in our winter runs where no plume exists, we dropped the background velocity to the default value of 0.1 m s$^{-1}$, although we lack observational constraints on this value.

All experiments were run in a hydrostatic configuration with a nonlinear free surface, 4 s time steps, and a Coriolis frequency of $1.22 \times 10^{-4}$ s$^{-1}$. We prescribe horizontal eddy viscosities according to a Smagorinsky scheme (Smagorinsky, 1963), using a Smagorinsky constant of 2.2. The nonlocal K-Profile Parameterization scheme (Large et al., 1994) was used to parameterize vertical mixing, with a background and maximum viscosity of $5 \times 10^{-4}$ and $5 \times 10^{-3}$ m$^2$ s$^{-1}$, respectively. We set diffusivities to zero, although some numerical mixing still exists due to advective truncation errors. All reported model output is averaged over one day of model time. Information regarding model validation can be found in the Supporting Information.

### 2.6. MITgcm TEF Plume Reflux Calculations

Following the work of MacCready et al. (2021), we calculate recirculation of the outflowing plume by coupling TEF (MacCready, 2011) to efflux/reflux theory (Cokelet & Stewart, 1985), which quantifies the net effect of mixing in estuaries without the need to resolve the mixing itself. Their framework assumes an estuarine system where turbulent mixing between inflowing and outflowing layers primarily occurs at constrictions, such as sills, that are separated by deep, advection-dominated basins, where mixing is negligible. Across each mixing zone, some portion, the efflux, of each layer will be transported to the next basin, while the remainder, the reflux, will be vertically transported to the opposing layer and recirculated to its original basin (Figure 2). Through mass and volume conservation, this process can be written as:

$$\alpha_{21} Q_1 + \alpha_{24} Q_4 = Q_2$$

$$\alpha_{21} S_1 Q_1 + \alpha_{24} S_4 Q_4 = S_2 Q_2$$

$$\alpha_{31} Q_1 + \alpha_{34} Q_4 = Q_3 \tag{1}$$

$$\alpha_{31} S_1 Q_1 + \alpha_{34} S_4 Q_4 = S_3 Q_3$$

where $S_i$ and $Q_i$ are tidally averaged flux-weighted salinities and tidally averaged volume fluxes, respectively. Subscripts designate transport layers, where layers 1 and 2 are the inflowing and outflowing layers oceanward of the mixing zone, respectively, and layers 3 and 4 are the inflowing and outflowing layers glacierward of the mixing zone, respectively (Figure 2). $\alpha_{ij}$ represents the percentage of layer $j$ that mixes into layer $i$. The solutions to 1 are:

$$\alpha_{21} = \frac{Q_2}{Q_1} \frac{S_2 - S_4}{S_1 - S_4} \qquad \alpha_{31} = \frac{Q_3}{Q_1} \frac{S_3 - S_4}{S_1 - S_4}$$
$$\alpha_{24} = \frac{Q_2}{Q_4} \frac{S_1 - S_2}{S_1 - S_4} \qquad \alpha_{34} = \frac{Q_3}{Q_4} \frac{S_1 - S_3}{S_1 - S_4}. \tag{2}$$

In this framework, conservation of mass and volume require:

$$\alpha_{21} + \alpha_{31} = 1$$
$$\alpha_{24} + \alpha_{34} = 1 \tag{3}$$

and

$$S_4 \leq S_2 < S_1$$
$$S_4 < S_3 \leq S_1. \tag{4}$$

In this study, we are primarily concerned with $\alpha_{34}$, the reflux of the outward flowing plume back into the fjord at each mixing zone.

As with MacCready et al. (2021), we calculate $S_i$ and $Q_i$ using the TEF framework (MacCready, 2011), which satisfies the Knudsen Relations and accounts for both tidal and subtidal transports (Burchard et al., 2018; Knudsen, 1900; MacCready, 2011). TEF transports are the horizontal equivalent of the efflux/reflux vertical fluxes, and are thus the compatible framework for quantifying exchange flow (MacCready et al., 2021). Salt and volume fluxes across a given TEF transect are divided into 1,000 discrete salinity classes, and are then tidally averaged using a 24-24-25 hr Godin filter. We calculated inward and outward transports using the dividing salinity method, an updated methodology for calculated TEF quantities that allows for multiple inflowing and outflowing layers, and has been shown to provide accurate results even in weakly stratified water (Lorenz et al., 2019; MacCready et al., 2018). The sum of all inflowing and outflowing salt and volume fluxes are given as $F_{in,out}$ and $Q_{in,out}$, respectively, and the associated flux-weighted salinities are $S_{in,out} = F_{in,out}/Q_{in,out}$.

We defined TEF transects on either side of each of the four sills (Figure 1d), which we assume to be the primary locations of mixing in LeConte Bay, apart from the subglacial discharge plume. Transects were parallel to either the $x$ or $y$ axis, and we used the corresponding perpendicular velocity, $v$ or $u$, for our flux calculations. TEF transports were then substituted into Equation 2, using $Q_{in} = Q_1$ and $Q_{out} = Q_2$ for the transect oceanward of the mixing zone, $Q_{in} = Q_3$ and $Q_{out} = Q_4$ glacierward of the mixing zone. The same substitution is done for $S_{in,out}$. As done in MacCready et al. (2021), we made minor adjustments to the TEF transports prior to calculation of Equation 2 so that Equations 1, 3 and 4 are satisfied. This step is necessary because TEF budgets are not exact, and some drift in salinity may occur within each section (MacCready et al., 2021). An error was assigned to each variable equal to the difference that it was adjusted, and the error was then propagated through Equation 2. The net error on $\alpha_{ij}$ due to these corrections amounted to no more than 0.3% of the reported value, although it was typically much lower.

Parameterization of melting icebergs has only recently been implemented in the MITgcm (Davison et al., 2020), and we have inadequate fjord-scale coverage of iceberg prevalence to include it in our model. Still, iceberg melt is likely the primary freshwater source in the winter, and its neglect in our model may lead to spurious TEF results in the winter. We, therefore, limit our winter TEF budgets to one neap tide experiment, which we expect

underestimates actual reflux values, due to the decreased baroclinic volume fluxes and increased salinity throughout the fjord (Davison et al., 2020).

### 2.7. Observed Inflow Composition

Although we lack the proper spatial and temporal data coverage to undertake efflux/reflux theory with our observations, we can use standard mixing equations to arrive at similar results. The shallow depth of S1 allows only the uppermost Frederick Sound water to enter LeConte Bay each tidal cycle, during which we expect some amount of mixing to occur across each sill with the outflowing plume (the combined outflow of subglacial discharge, entrained ambient fjord water, iceberg melt, and surface runoff). Assuming these two end-members remain constant for the duration of a field campaign, and that no other water masses significantly contribute to the inflow, we can use conservation of mass, salt, and temperature to write the inflowing $\theta/S$ properties as a mixing product of Frederick Sound ($fs$) and plume ($plm$) water:

$$\chi_{fs} + \chi_{plm} = 1$$
$$\chi_{fs} S_{fs} + \chi_{plm} S_{plm} = S_{in} \tag{5}$$
$$\chi_{fs} \theta_{fs} + \chi_{plm} \theta_{plm} = \theta_{in}$$

where $\chi$ is the fraction of Frederick Sound or refluxed plume water within a water parcel in the glacierward flow. Equation 5 can be rearranged to solve for $\chi_{plm}$:

$$\chi_{plm} = \frac{S_{fs} - S_{in}}{S_{fs} - S_{plm}}. \tag{6}$$

We use CTD and ADCP data from August 2016 at repeated transects across S3, together with CTD casts in Frederick Sound (Figure 1) to calculate ($\theta_{plm}$, $S_{plm}$) and ($\theta_{in}$, $S_{in}$); other surveys lacked adequate data in Frederick Sound. For each transect, we used the 150 kHz ADCP to isolate the plume (defined as outflowing water within the $-0.03$ m s$^{-1}$ contour in contact with the maximum outward surface velocity) from the inflow, then found the mean ($\theta_{plm}$, $S_{plm}$) across all transects. As only the shallowest Frederick Sound water can pass over S1, we averaged only the upper 29 m of Frederick Sound CTD casts to determine ($\theta_{fs}$, $S_{fs}$). This is the depth of the 90% contour of the Frederick Sound passive tracer remaining in Frederick Sound at the end of our neap tide MITgcm scenarios (the tidal phase during the August 2016 survey).

For each transect, we then calculate the net, volume flux-weighted percentage of plumewater in the inflow:

$$X_{plm} = \frac{\int_A \chi_{plm} u' \, dA}{\int_A u' \, dA} \qquad \text{for} \quad u' > 0 \tag{7}$$

for glacierward baroclinic velocity $u'$ and cross-sectional area $A$. This calculation requires extrapolating $\chi_{plm}$ and $u'$ to the sides, bottom, and surface of the fjord. To ensure conservation of volume, we follow similar steps to Sutherland et al. (2019a) in which we extrapolate to the surface assuming constant shear, then arbitrarily add the missing volume flux uniformly (a) to all depths, (b) to the inflow at 50–165 m depth, (c) to the intensified inflow at 125–165 m depth, or (d) to the surface layer at 0–50 m. The range in these scenarios is then incorporated into the uncertainty in $X_{plm}$, together with the uncertainty in $\chi_{plm}$.

## 3. Results

### 3.1. Observed Seasonal Stratification and Circulation Regimes

Shipboard and mooring data depict two dominant stratification and circulation regimes in LeConte Bay: (a) a winter regime (November–March) with a weak two-layer exchange flow that occurs when subglacial discharge is negligible, and (b) a highly stratified, three-layer summer regime (mid-June–mid-September) when mean subglacial discharge is between 150 and 400 m$^3$ s$^{-1}$ (Figures 3 and 4). Two short transitional periods in spring (April–mid-June) and fall (mid-September–October) bridge these two regimes, and represent the establishment or destruction of stratification, coincident with the initiation or cessation of subglacial discharge, respectively.
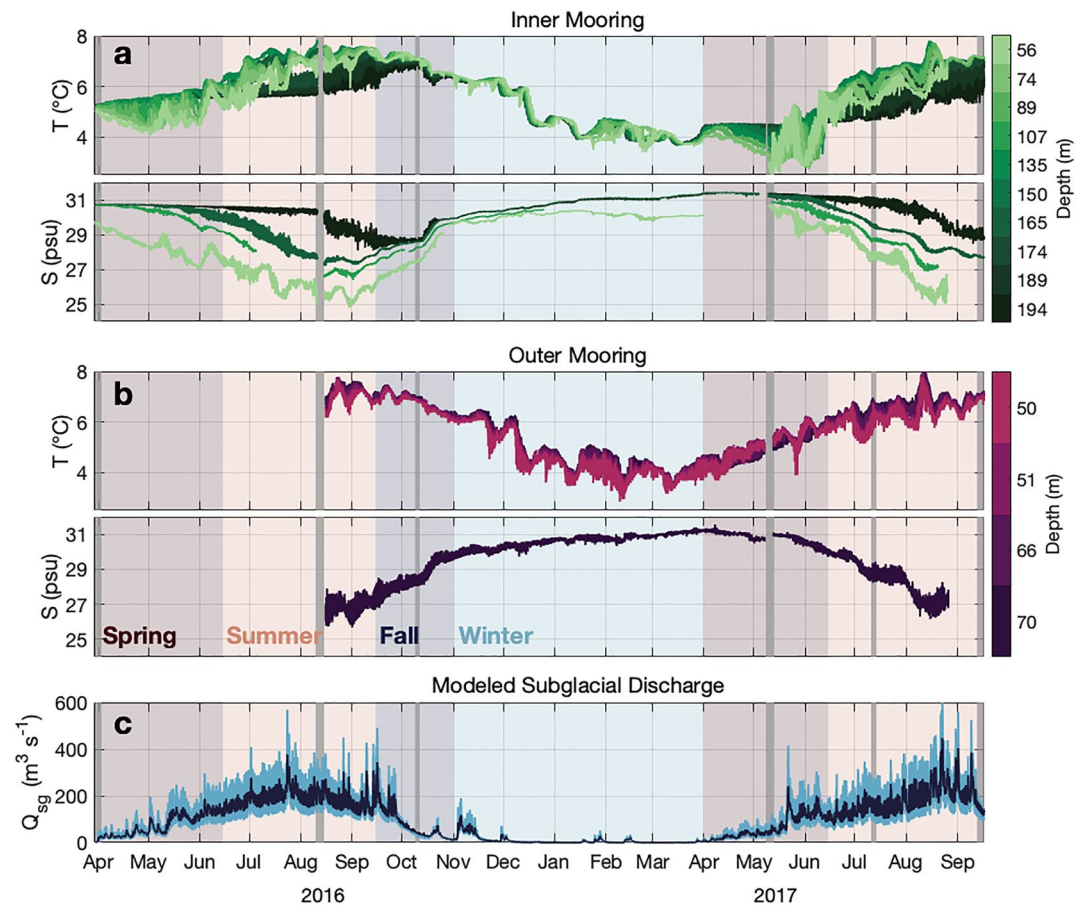
**Figure 3.** Temperature and salinity time series from (a) the Inner Mooring and (b) the Outer Mooring, color-coded by depth of each instrument. The Inner Mooring comprised of 10 temperature instruments, four of which also recorded salinity. All four Outer Mooring instruments measured temperature, and one also recorded salinity. (c) Modeled subglacial discharge for our study period, depicting the range in runoff scenarios in light-blue, and the medium runoff scenario in dark-blue. Gray bars in (a–c) indicate shipboard surveys. Background colors demarcate the four seasonal regimes and transitional periods.

### 3.1.1. Seasonal Water Properties and Stratification

Mooring and CTD $\theta/S$ data revealed that water properties were largely homogeneous both vertically and horizontally throughout most of the winter (Figures 3 and 4). Both moorings had only minor salinity fluctuations throughout November–March, except for a gradual increase of ~1.5 psu measured at all instruments (Figure 3). The entire fjord experienced fortnightly temperature cycles reflecting spring/neap tidal forcing, which were superimposed over a general cooling trend of ~3°C throughout the winter. CTD casts from late winter (March/April 2016) depict a cold, fresh surface layer in the upper 10 m that transitioned into a continuously stratified water column until 100 m depth, below which was nearly homogeneous water (Figure 4a). Despite the weak horizontal gradients within the fjord, winter $\theta/S$ properties differed by an average of ~3.5°C and 1 psu across S1.

Stratification started to develop almost immediately upon the onset of subglacial discharge in early April of both years, marking the beginning of the spring transitional period. In 2017, Inner Mooring temperatures cooled between 50 and 130 m throughout April, while Outer Mooring temperatures warmed (Figure 3). This opposing behavior created a large along-fjord temperature gradient across B2 in the upper 150, although along-fjord salinity gradients remained negligible (Figure 4). At this time, a warm glacierward intrusion was observed at 25–50 m depth in B2 (Figure S5 in Supporting Information S1). In early/mid-May, Inner Mooring temperatures started their annual warming trend, reaching similar temperatures to the Outer Mooring by late May to early June. Warming at the Inner Mooring began with its shallowest sensors and gradually deepened to ~165 m, where
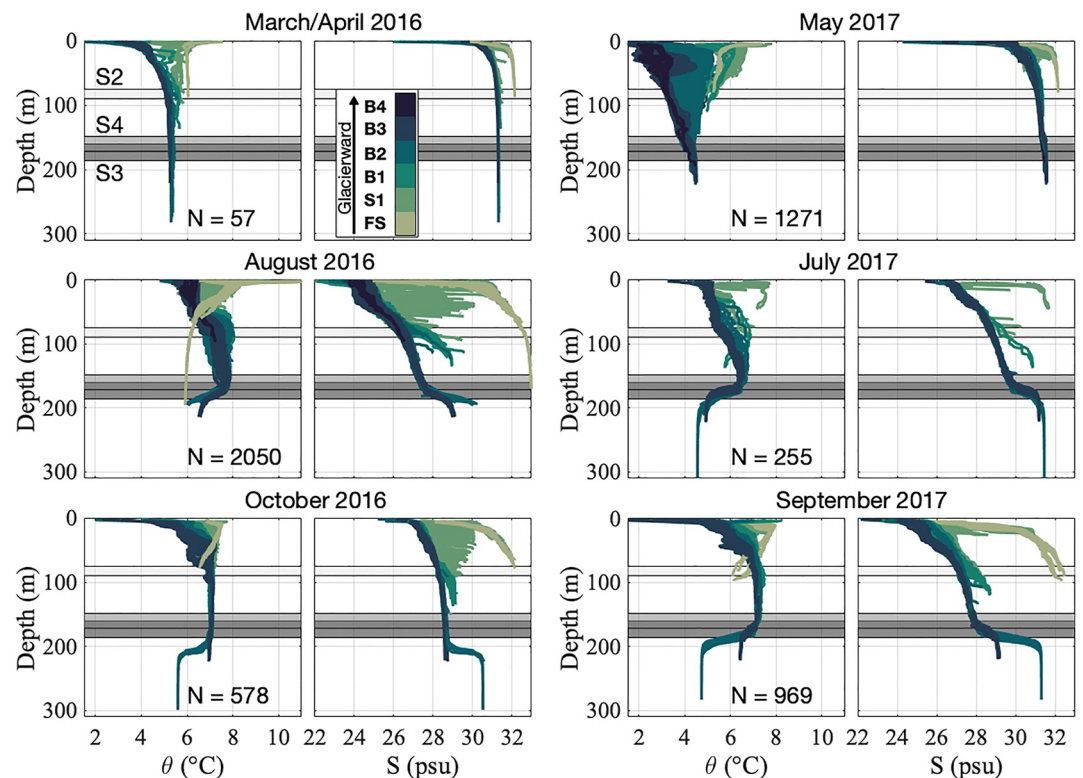
**Figure 4.** $\theta/S$ data from all CTD casts during each field campaign, color-coded by location in Frederick Sound (FS), over S1, or within each sub-basin. Horizontal gray bars depict the depths of S2, S3, and S4.

the warmest water resided by the end of the transitional period. Below this depth, temperatures remained fairly constant.

Summer stratification began in mid-June of both years, and marked the development of a highly stratified, three-layer system, as seen in all of our summer surveys (August 2016, July 2017, September 2017; Figure 4). The upper ~50 m of the water column was a relatively cold (5°C–6°C) and fresh (24–27 psu) surface layer. A pycnocline at ~50 m separates this layer from a warm (6°C–8°C) water body at 50–165 m. The warmest water in the fjord was within this layer and consistently occurred between 120 and 165 m depth. A prominent second pycnocline existed in B2 and B3 at 165–185 m, which coincided with the depths of S3 and S4 (Figure 4 and Figure S3 in Supporting Information S1). CTD surveys conducted at different months of the summer show this pycnocline strengthened throughout the summer, as overlying water freshened and warmed. Below the 165–185 m pycnocline rests a third water mass with the same $\theta/S$ properties as winter deep water. In the shallower B1 basin, a less dramatic pycnocline at ~90 m, corresponding to the depth of S2, separated the middle layer from a saltier and colder bottom layer (Figure 4). As a result of the 90 m and 165–185 m pycnoclines, water properties bifurcated at each sill (S2–S4), so that water below sill depth was warmer and fresher on its glacierward side.

Large internal tides were recorded at the Inner Mooring within and just below the 165–185 m pycnocline (Figure S4 in Supporting Information S1) that amplified throughout the summer as the pycnocline strengthened. At their largest, these internal tides created semi-diurnal fluctuations of up to 1.5°C and 1 psu, indicating a maximum wave height of 35 m.

### 3.1.2. Seasonal Circulation

External water enters LeConte Bay from Frederick Sound via unidirectional flow over S1 each flood tide. Warm, dense Frederick Sound water then propagates down the lee-side of S1 as a gravity current upon entering LeConte Bay (Figure 5). During our March/April 2016 survey, a salinity difference of 1 psu between external and ambient water resulted in a gravity current of $\leq$0.5 m s$^{-1}$, which formed a hydraulic jump upon reaching neutral buoyancy at ~50 m depth. In contrast, fresher ambient fjord conditions (and an across-S1 salinity difference of 6 psu) in
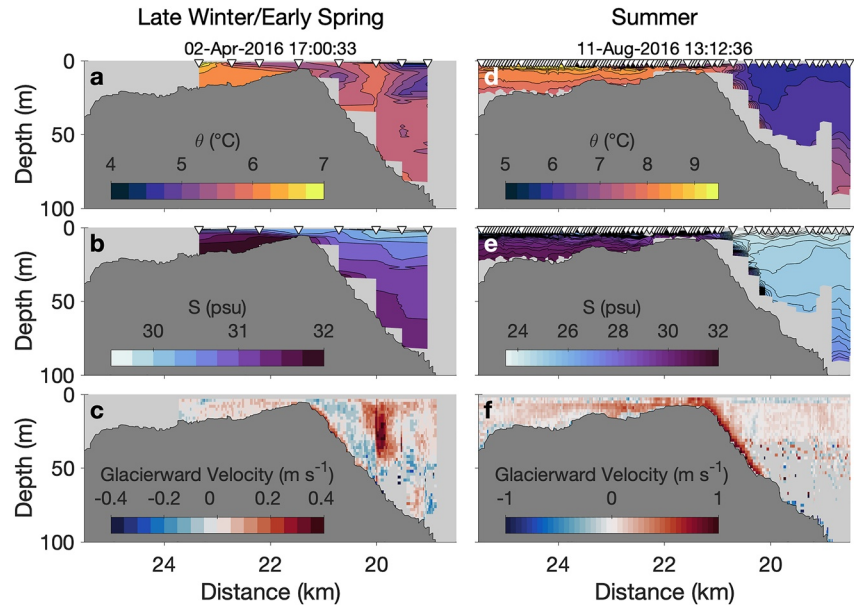
**Figure 5.** Shipboard CTD and ADCP transect over S1 from late winter/early Spring (April 2016) and summer (August 2016). Both transects were measured during neap flood tides, and the median time of each transect is given. White triangles in (a, b) and (d, e) mark the location of each CTD cast, which are also shown in Figure 1. Note the differing color-scales between surveys. View is to the north (Frederick Sound to the left and LeConte Bay to the right).
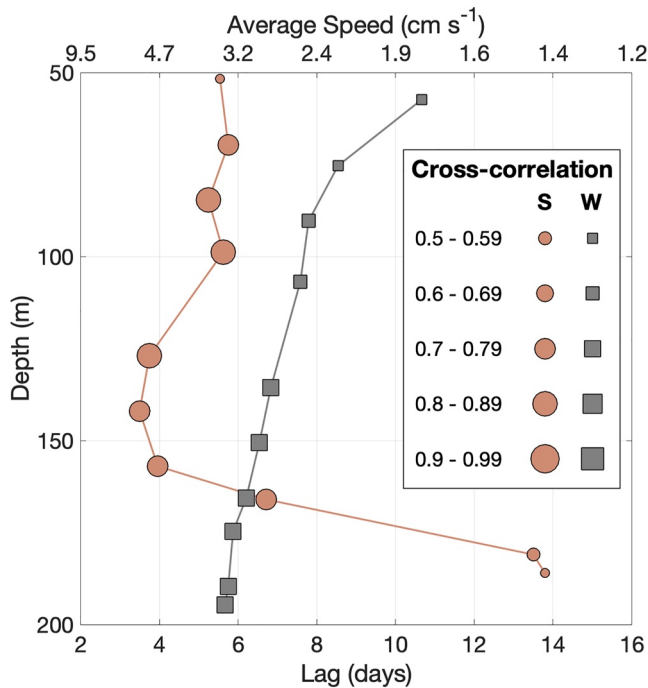


**Figure 6.** Time-lagged cross-correlations between each of the Inner Mooring temperature sensors and the uppermost Outer Mooring temperature sensor (50 m). Markers indicate the lag time (and inferred travel speed) with the highest correlation for each sensor. Circles and squares represent mooring data summer (15 June to 15 September) 2017 and winter (1 November to 31 March) 2016–2017, respectively. Marker size scales with maximum correlation of each instrument. All correlations are significant.

August 2016 created flood tide gravity currents that traveled up to 1 m s$^{-1}$ to a depth beyond the range of our ADCP (Figure 5); however, CTD casts suggest these flows reached neutral buoyancy near the 90 m pycnocline in B1.

To determine the fate of water after it enters LeConte Bay, we used time-lagged cross-correlations between the Inner Mooring temperature sensors and the Outer Mooring temperature sensor deployed at 50 m depth (based on the MITgcm experiments, all flow to the Inner Mooring sensors would have first traveled near this instrument). As salinity largely controls fjord density, temperature is the better tracer of water masses, and the larger number of temperature sensors on each mooring greatly increases vertical resolution. Cross-correlations were calculated between instruments at lag intervals of 1 hr, and we report only the lag time with the strongest correlation (cross-correlations had only one significant maximum). In the winter, the deepest Inner Mooring sensor had the strongest correlation with the Outer Mooring ($r = 0.73$). This sensor also recorded the shortest lag time between moorings (5.7 days), implying an average travel speed of 3.3 cm s$^{-1}$ between moorings (Figure 6). Correlations decreased and lag times increased for each successively shallower sensor in the water column. During the summer of 2017, the three shortest lag times of 3.7–4 days, suggesting mean speeds of 4.6–5.2 cm s$^{-1}$, were recorded between 125 and 160 m depth, just above the 165–185 m deep pycnocline. This depth also coincided with the warmest water observed in the summer Inner Mooring record and CTD surveys. Below the pycnocline, lag times dramatically increased with depth to >14 days. Lags in the upper inflowing layer, between 50 and 100 m depth, varied from 5.4 to 5.9 days, suggesting mean travel speeds of 3.2–3.4 cm s$^{-1}$. All temperature sensors between 70 and 166 m depth exhibited moderate to strong correlations ($r > 0.7$) between moorings.
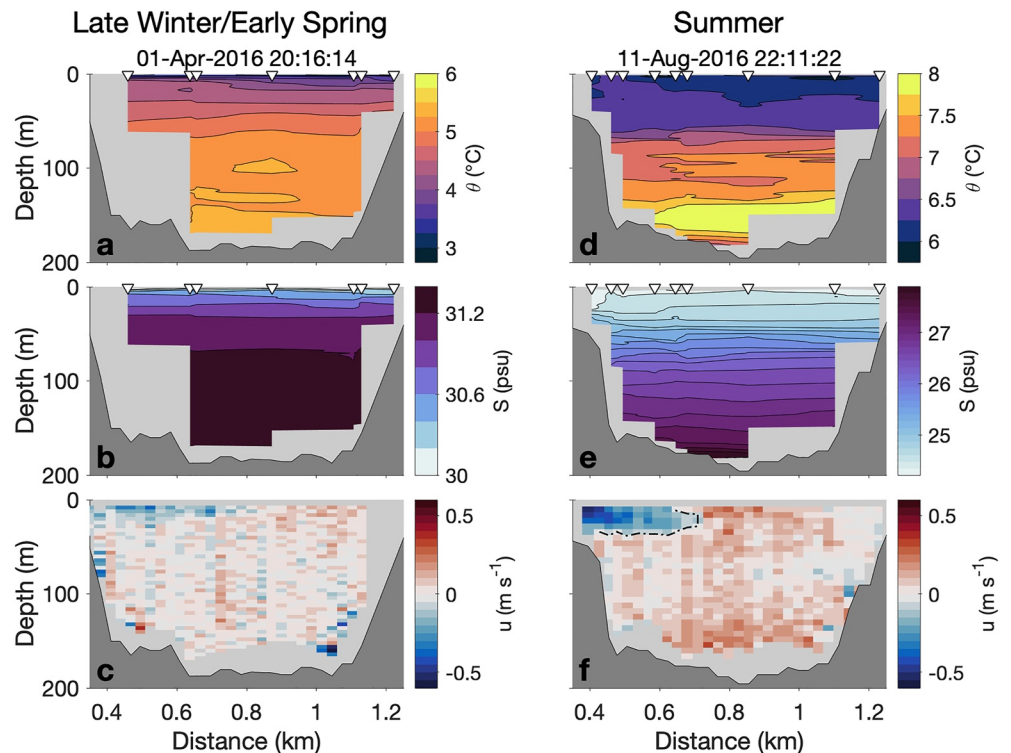
**Figure 7.** Shipboard CTD and ADCP transect along S3 in late winter/early spring (April 2016) and summer (August 2016), both measured during neap ebb tides (median time of each transect is given). Positive velocities are glacierward. The −0.03 m s$^{-1}$ contour used to distinguish the plume in our observed reflux calculations is shown in (f). White triangles in (a, b) and (d, e) mark the locations of each CTD cast, which are also shown in Figure 1. Note the differing color-scales between surveys. The view is glacierward.

Figure 7 depicts typical across-fjord transects over S3 from March/April 2016 and August 2016, and illustrates the main differences between the winter and summer circulation regimes. In the winter, a weak estuarine exchange flow existed within the surface layer, including a small outward flowing plume on the north bank of the fjord. The plume was compensated primarily by surface inflow along the fjord's south side, as well as slow-moving, homogeneous water at depth. Note that some subglacial discharge was present during this survey, which contributed to the plume's volume. Conversely, surface exchange flow in the summer occurred in the upper 50 m, and instantaneous water velocities were approximately 2–3 times greater than in winter. Again, the outflowing plume was located on the fjord's north bank, and was partly compensated by an estuarine exchange flow to the south. However, a comparable inflow existed 120–165 m deep that contains the warmest (<8°C) water observed at the Inner Mooring and in all summer CTD casts. This is also the depth where the shortest lags were calculated in mooring cross-correlations. In August 2016, the surface exchange flow in the upper 50 m and the heightened inflow at 120–165 m each accounted for 29% of the inflowing volume flux at S3, despite occupying only 13% and 10% of the cross-sectional area, respectively. Just below the intensified, warm inflow is the 165–185 m pycno-cline, which is obscured in Figure 7 by S3 bathymetry, but visible in Figure S5 in Supporting Information S1.

## 3.2. MITgcm Fjord Circulation

Modeled water velocities largely agreed with observations and provide insight to fjord-scale circulation (Figure 8). In winter experiments, unidirectional tidal flows forced Frederick Sound water into LeConte Bay, creating grav-ity currents of similar speed (~0.5 m s$^{-1}$) to those observed (Figures 5c and 8c). In the poorly stratified winter water column, weak gravity currents then propagated down S1 and S2 to the floor of B2 (~320 m), renewing the deepest fjord water first before the overlying water column (Figure 8, Movie S1). This circulation style agrees with evidence from mooring cross-correlations, and tidally averaged model velocities were of similar magnitude to those estimated from correlation lag times. The modeled tidally averaged outflow was deeper than the surface
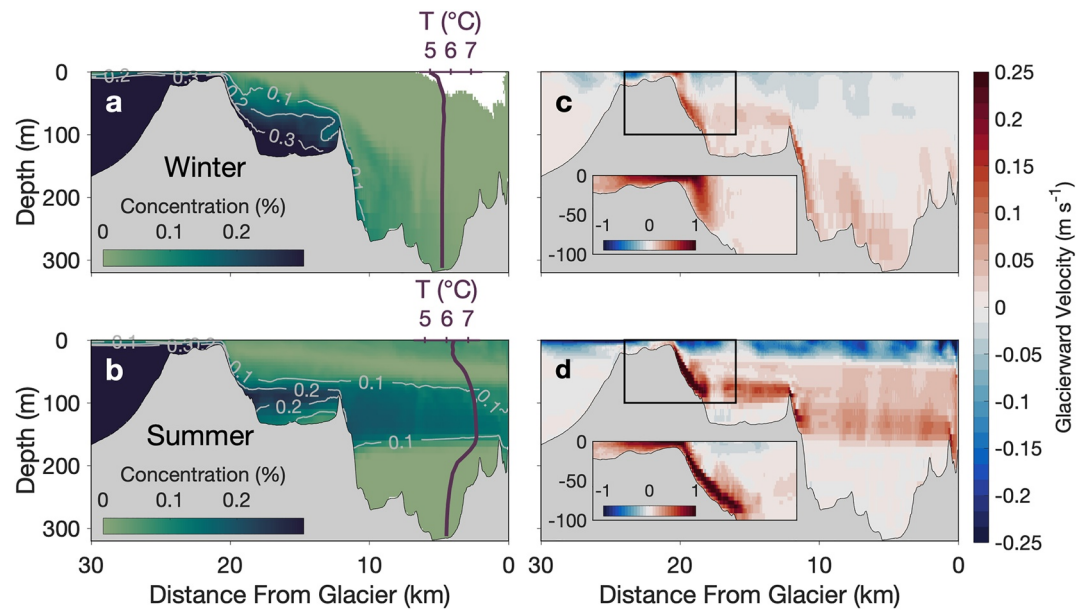
**Figure 8.** MITgcm tidally averaged, thalweg Frederick Sound passive tracer concentrations and glacierward velocities for (a, c) winter and (b, d) summer experiments. Tracer concentrations are plotted 7 days after tracer initialization. Purple lines in (a, b) are temperature profiles extracted from B2. Insets in (c, d) depict instantaneous velocities across S1 (black box) during maximum flood tide. Note the different color-scale used in the insets. The summer run used in (a) and (c) was forced with neap tides and subglacial discharge of 250 m³ s⁻¹.

exchange observed in March/April 2016, but it is unclear if this is an accurate portrayal of winter circulation, or an artifact of neglecting subglacial discharge and iceberg meltwater.

In our summer scenarios, gravity currents entered LeConte Bay from Frederick Sound at velocities of ~1m s⁻¹ (Figure 8d), consistent with shipboard transects across S1 (Figure 5f). Instead of sinking to the bottom of B1 and B2, summer gravity currents traveled along the pycnoclines formed oceanward of S2 and S4. These are the same 90 m and 165–185 m pycnoclines observed in summer surveys, below which rested stagnant water in both the model and observations. Above each pycnocline, where gravity currents reached neutral buoyancy, was a band of fast inflowing water (at 120–165 m depth in B2; Figure S2 in Supporting Information S1) with tidally averaged velocities similar to those estimated from mooring cross-correlations (Figure 8d). This depth also contained the highest concentration of Frederick Sound water in our model, and was where the fastest and warmest inflowing water exists in the summer (Figure 8b). In our model, the warm, high Frederick Sound concentration water over-topped S4, and was drawn down to the glacier grounding line. It was then entrained into the subglacial discharge plume and exported from the glacier terminus in a 40 m deep surface layer (Movie S1).

### 3.3. Plume Reflux Calculations

#### 3.3.1. Observed Inflow Composition

On average, 66% ± 18% of the inflow observed at S3 in August 2016 was composed of refluxed plume water (Figure 9d). As expected, the greatest percent (50%–80%) of refluxed plume water resided in the slow inflow at 50–125 m depth, while the enhanced inflow at 125–165 m depth still consisted of 30%–50% plume water (Figure 9a). Below 165 m depth, $\theta/S$ properties drift from the Frederick Sound-plume mixing line, indicating the water within and below the 165–185 m pycnocline is mixed with an additional water body, and contains very little recirculated plume water. This third $\theta/S$ signature is consistent with winter deep water.

#### 3.3.2. TEF Reflux in MITgcm Experiments

Across all summer runs, 57%–70% of the outflowing plume was refluxed at the S1 (Figure 9b), and plume reflux at all other sills was negligible (<3% and often <1%). The addition of subglacial discharge decreased the fraction of the plume that was refluxed at S1 ($\alpha_{34}$); however, because the plume was larger in higher subglacial discharge
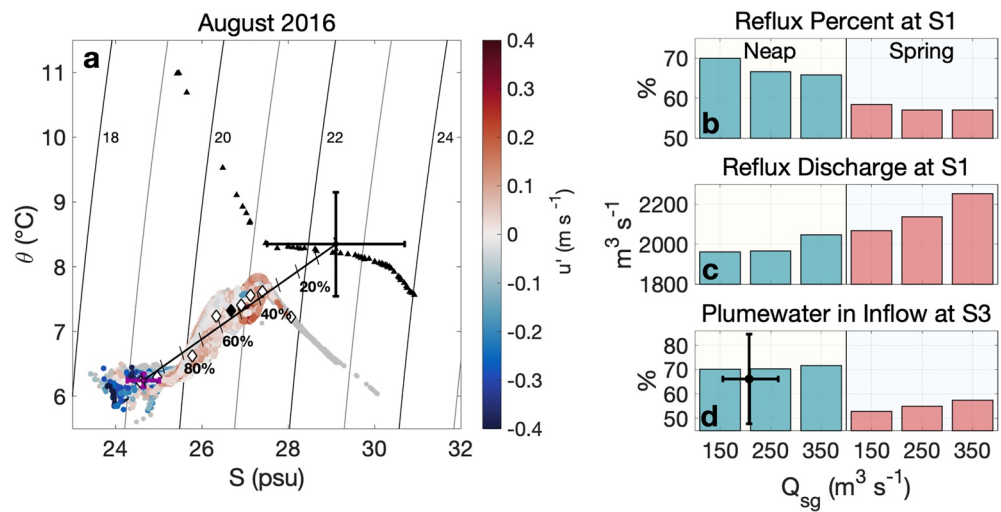
**Figure 9.** (a) $\theta/S$ data from CTD casts along S3 (circles) and upper Frederick Sound water (black triangles) used to calculate $\chi_{plm}$ and $X_{plm}$. S3 CTD casts are color-coded by glacierward baroclinic velocity, as measured from the 150 kHz ADCP. Gray circles indicate data points without corresponding velocities. Standard deviations of Frederick Sound and plume water properties, used to calculate uncertainty in $\chi_{plm}$, are given as the black and purple error bars, respectively. The mixing line connecting the two end-member means illustrates the percentage of plume water throughout the inflow ($\chi_{plm}$). Diamonds indicate depth intervals of 20 m; the black diamond is at 100 m. Contours denote density anomaly. (b) The reflux percent ($\alpha_{34}$) and (c) reflux discharge ($Q_R$) at S1 for all summer MITgcm runs, plotted by forcing magnitude. (d) The fraction of plume water in the inflow at S3 in all summer MITgcm runs, plotted with the average $X_{plm}$ (black error bars) for all transects in (a). Note the average $X_{plm}$ is plotted with the neap tide model scenarios to represent the tidal phase during the field survey.

scenarios, this still corresponded to an overall increase in the volume flux of recirculated plume water ($Q_R$) at S1 (Figures 9b and 9c). Conversely, stronger tidal forcing decreased $\alpha_{34}$, yet still led to a higher $Q_R$ than neap tide runs. In all summer runs, a greater reflux volume at S1 led to decreased inflowing salinity and near-glacier temperatures for a given tidal forcing (Table S1 in Supporting Information S1). In total, refluxed plume water accounted for 53%–72% of inflowing water by the time it reached S3 (Figure 9b). This was determined by treating the section of the fjord between S3 and Frederick Sound as one mixing zone (Cokelet & Stewart, 1985), and calculating the reflux budget using the oceanward S1 transect and the glacierward S3 transect (Figure 1d). $\alpha_{34}$ was higher in our winter experiment than any summer run, reaching 74% at S1 and 8.5% at S2 (Table S1 in Supporting Information S1). Still, due to the weaker water velocities and lack of subglacial discharge, $Q_R$ was on average only 34% of summer runs at S1.

As a point of comparison, we also quantified the impact of shear-driven mixing independent of sills, which we calculated by treating B2 as its own mixing zone. Three percent or less of the surface plume was refluxed across B2, comparable to reflux at the three deepest sills. However, up to 10% of the inflow was entrained into the surface plume, indicating the plume continues to grow even after reaching neutral buoyancy.

# 4. Discussion

Our results demonstrate the importance of coupled sill-generated mixing and subglacial plume-driven buoyancy forcing in promoting substantial seasonal differences in fjord circulation. Such seasonal circulation regimes are important drivers of heat advection at LeConte Bay and likely other glacial fjords.

## 4.1. Seasonal Circulation and Stratification Regimes

### 4.1.1. Winter Regime (November–March)

In the winter, when subglacial discharge is negligible, fjord renewal and circulation in LeConte Bay is analogous to a non-glacial silled fjord. Large tidal velocities of ∼1 m s$^{-1}$ across S1 overwhelm any baroclinic transport across the sill, and thus the timing and volume of renewal events is largely dependent on the tidal prism (e.g., Gade & Edwards, 1980; Geyer & Cannon, 1982; Stigebrandt, 1977). Due to the reflux of glacial and iceberg
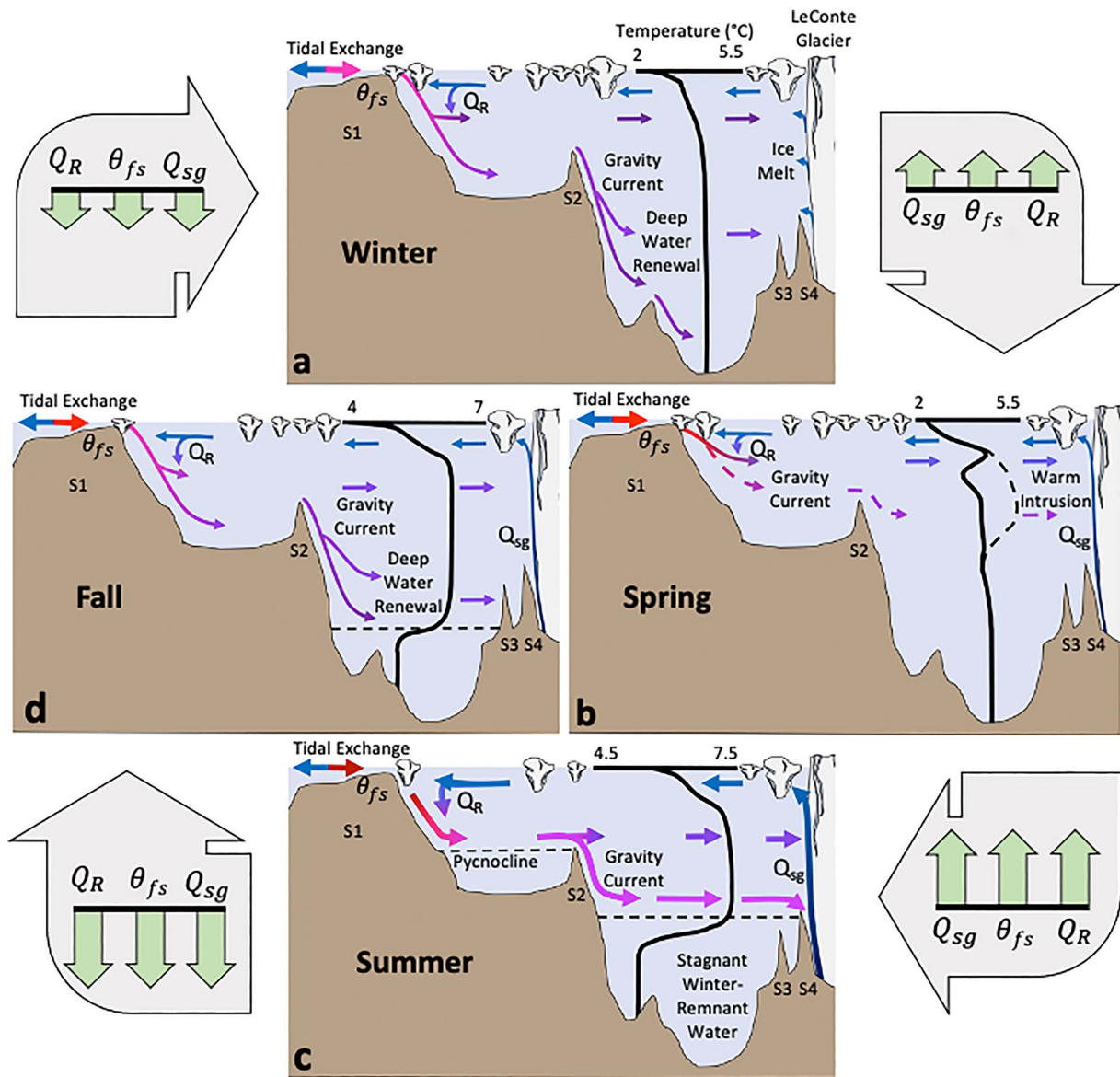
**Figure 10.** Schematics of characteristic along-fjord circulation patterns for each season, along with approximate temperature profiles in B2 (note the differing temperature ranges). Colors of arrows in (a–d) represent relative water temperatures. Dashed lines in (b) indicate the progressive deepening of inflowing water throughout the spring transition, as inferred from the Inner Mooring record. Large gray arrows in corners qualitatively depict the trends in subglacial discharge ($Q_{sg}$), Frederick Sound temperature ($\theta_{fs}$), and reflux discharge ($Q_R$) between seasons.

meltwater at S1, LeConte Bay remains fresher than Frederick Sound throughout the winter, which allows renewing water to sink to depth.

Once over S1, renewing water flows glacierward down S1 and S2 as a gravity current until reaching the bottom of the fjord (Figure 10a), as evident in our winter MITgcm experiments (Figure 8) and mooring time-lagged cross-correlations. Winter transit times from S1 to the glacier terminus may be upwards of 10 days (Figure 6), although the water with the highest Frederick Sound concentration is routed to depth in B2 (Figure 8a). B2 deep water may eventually be replaced by denser renewing water, reaching the glacier terminus only after some amount of uplift, mixing, and dilution.

In the absence of an appreciable freshwater source in the winter, renewing water properties appear to be determined by two main processes: (a) the volume of Frederick Sound water forced over S1 each flood tide, and (b) the $\theta/S$ of Frederick Sound water. Frederick Sound is warmer than LeConte Bay throughout the year (Figure 4),

and thus differences between spring and neap tidal volume fluxes create fortnightly fluctuations in LeConte Bay, with warming occurring during spring tides (Figure 3). The relatively minor difference in salinity between these two water bodies in the winter (1 psu) explains why only minimal fortnightly fluctuations in salinity are observed.

### 4.1.2. Spring Transitional Period (April–mid-June)

The spring transition began when subglacial discharge accelerated at the beginning of the melt season, causing additional mixing and reflux of freshwater at S1. At LeConte Bay, this happened in early April during both years of our study. Almost immediately, renewal of deep water ceased (Figure 3), and the fjord entered a temporary transitional period in which a large along-fjord temperature gradient developed across B2 in May 2017 (Figure 4). We posit that a similar process to what has been observed at Loch Sunart, Scotland (Gillibrand et al., 1995), occurred at this time. Initially, the additional freshwater reflux freshened inflowing water so that it was less dense than ambient fjord water, thus creating a stratified surface layer that prevented deep water renewal, despite the presence of subglacial discharge. Inflowing water instead flowed glacierward near the surface, creating the warm intrusion at 25–50 m depth observed in May 2017 (Figure S5 in Supporting Information S1). Below this depth, advection was weak and a strong along-fjord temperature gradient developed (Figure 4). However, as subglacial discharge increased throughout the spring, so did the reflux of freshwater at S1. As with Loch Sunart, freshwater reflux eventually freshened fjord conditions enough to allow renewing water to again sink gradually deeper in the water column (Gillibrand et al., 1995). At LeConte Bay, the Inner Mooring time series depicts the top-down freshening and cooling of the fjord in April, followed by warm intrusions in May that progressively occur deeper in the water column (Figure 10b).

Entrainment of ambient fjord water into the subglacial plume expedites this fjord renewal process (Carroll et al., 2017; Gladish et al., 2015), and allows for dense winter water to be readily replaced by progressively fresher water throughout the melt season. However, water below the glacier's grounding line depth, or oceanward of any obstructing secondary sills, cannot be entrained and renewed, leading to its isolation and stagnation in the spring and summer. Eventually, all water above grounding line depth that can be renewed is replaced by fresher water, creating pycnoclines at grounding line depth or at the depth of obstructing sills. It is above these pycnoclines where summer gravity currents will reach their terminal depth and flow glacierward. In LeConte Bay, this occurs at 90 m depth in B1 and 165–185 m depth in B2, as determined by the depths of S2 and S3/S4, respectively.

### 4.1.3. Summer Regime (mid-June–mid-September)

We define the beginning of the summer regime as the time when freshwater reflux and plume entrainment have permitted renewing gravity currents to reach their terminal depth above S3 and S4, and establish the 165–185 m pycnocline (Figure 10c). This occurred in mid-June of both years (Figure 3). In B2, gravity currents reached neutral buoyancy at 120–165 m, where the fastest glacierward velocities, warmest water, and highest concentrations of Frederick Sound water occurs in the summer (Figures 8 and 9a). MITgcm experiments indicate that the draw down of water from S4 to the grounding line via plume-driven entrainment creates a subcritical flow over S4 that augments velocities on its oceanward side (Figure 8d). It seems likely that this process, together with the momentum carried by gravity currents reaching neutral buoyancy at the same depth, are responsible for the enhanced velocities observed at 120–165 m. An estuarine exchange flow in the upper 50 m was also prevalent throughout the summer (Figure 7).

At S1, the ~40 m deep outflowing plume was largely blocked by the shallow sill, creating conditions that could lead to overmixing (Stigebrandt, 1981; Stommel & Farmer, 1953), if not for the strong barotropic tides forcing semi-diurnal exchange with Frederick Sound. The intersection of the plume with S1, paired with fast tidal currents (0.5–1 m s$^{-1}$; Figures 5 and 8), readily mixed outflowing plume water with inflowing Frederick Sound water. Both MITgcm TEF experiments and August 2016 $\theta/S$ observations indicate enough mixing occurs at S1 to cause a majority of the outflowing plume to be recirculated, and subsequently make up the bulk of the inflow. TEF budgets indicate salinities decrease and reflux volumes increase with additional subglacial discharge. Therefore, as subglacial discharge increases throughout July and August, the larger volume of ambient water entrained into the subglacial discharge plume will be replaced by a reciprocal supply of continually fresher renewing water. This creates a cycle of continuous freshening of fjord water and strengthening of pycnoclines (Figure 4) until a steady-state is reached, or until subglacial discharge subsides in the fall.

Approximately 10% more of the outflowing plume was expelled from the fjord during spring tide model scenarios. However, by volume, more plume water was refluxed during spring tide, which was on average 1 psu saltier

than neap tide plume water. This is the result of larger barotropic volume fluxes over S1, as well as throughout the fjord. Such tidal dependence of reflux volume and salinity explains the fortnightly salinity cycles observed in the mooring record.

Summertime stratification prevents deep water (>185 m) renewal by gravity currents in B2, and deep water properties in B2 largely maintained their winter signatures throughout both summers (Figures 3 and 4). However, the gradual freshening and warming of the deepest Inner Mooring sensors indicate the upper deep water may undergo some renewal through mixing generated by internal tides, although the persistence of water properties below 200 m indicates wave-generated renewal is limited.

We can attribute the variations in summertime water properties in LeConte Bay to three primary forcing mechanisms: (a) $\theta/S$ properties of Frederick Sound, (b) strength of tidal forcing, and (c) subglacial discharge. During both summer and winter, tidal forcing regulates the volume of external water entering the fjord; however, when paired with summer subglacial discharge, tidal magnitude is the dominant control on the recirculation of large volumes of freshwater back into the fjord. Buoyancy forcing related to subglacial discharge drives an along-fjord circulation at depth (Motyka et al., 2003), and helps draw Frederick Sound water down each sill toward the grounding line (Carroll et al., 2017). However, our results indicate that in fjords where heavy mixing between layers promotes large reflux volumes, subglacial discharge will also have a substantial impact on the composition of the inflow. Variations in subglacial discharge will therefore affect both the magnitude of the buoyancy-driven flow toward the glacier, as well as the water properties of the inflow.

### 4.1.4. Fall Transitional Period (mid-September–October)

The fall transition begins with the attenuation of subglacial discharge, which started in mid-September of both years. By the end of October, the water column is almost entirely homogenized (Figure 3), except for a remnant of the 165–185 m pycnocline now below the Inner Mooring at 200 m (Figure 4). The rapid destruction of stratification illustrates the precarious balance between freshwater reflux and tidal renewal of external water. Without the reflux of substantial volumes of subglacial discharge and associated meltwater, summertime stratification quickly collapses, and circulation reverts to its winter regime. As inflowing water increases in density, gravity currents propagate deeper into B2, gradually weakening the remnant summer pycnocline and sinking it deeper into the water column (Figure 10d).

### 4.2. Implications for Heat Transport to LeConte Glacier

Multiple lines of evidence indicate heat transport to LeConte Glacier is enhanced during the summer circulation regime, and may become more pronounced with future changes in local climate. First, summertime circulation creates a direct pathway for the warmest water of Frederick Sound, found at its surface, to reach the LeConte Glacier grounding line at 200 m depth, 25 km away. Throughout the summer, heightened along-fjord water velocities rapidly transport Frederick Sound surface water to the glacier terminus within 4–5 days, where only the warmest water (>7°C) reaches the grounding line. Summer submarine melt rates of 8 m d$^{-1}$, the highest observed at LeConte Glacier, coincide with the depth of this intrusion (Sutherland et al., 2019a). Upon reaching the terminus, this warm water is entrained into the subglacial discharge (Motyka et al., 2013, 2003) and meltwater plumes (Jackson et al., 2020), and vertically displaced along the glacier terminus. Conversely, in the winter, the highest concentration of Frederick Sound water flows to the bottom of B2, and may only reach the glacier through further mixing and dilution with overlying water.

Second, the majority of the outflowing plume is refluxed at the fjord mouth, which significantly increases the flushing time of LeConte Bay. This is supported through a simple flushing time calculation developed for tidally flushed estuaries (Sanford et al., 1992), which we use for each of our MITgcm scenarios:

$$t_f = \frac{V\,T_{tide}}{(1-b)\,V_{fl} + V_{fw}} \tag{8}$$

where $V$ is the fjord volume, $T_{tide}$ is the tidal period, $V_{fl}$ is the flood tidal prism, $V_{fw}$ is the freshwater volume flux (equivalent to subglacial discharge), and $b$ is a return flow factor analogous to $\alpha_{34}$ at S1. Applying this model to LeConte Bay, we consider the entire fjord volume for our winter run, while for summer runs, we only consider the volume of water above 185 m that undergoes renewal. Summer flushing times more than double from 5 to

11 days if neglecting reflux ($b = 0$) to 11–32 days when reflux is accounting for ($b = \alpha_{34}$; Table S1 in Supporting Information S1). In winter, accounting for reflux increases the fjord flushing time from 22 to 77 days. This indicates reflux may extend the duration of synoptic temperature anomalies within LeConte Bay and delay the export of glacial freshwater to the coastal ocean.

Third, the internal tides observed in both summers suggest such waves may be important to the heat balance of the glacier terminus. Internal tides commonly form near sills, and become particularly pronounced when pycnoclines coincide with sill depth (Gade & Edwards, 1980), as is the case for summer pycnoclines in LeConte Bay. Internal waves may influence the composition of near-glacier water through vertical mixing, or by regulating which water masses flow into B4 (deep water or overlying renewing water). Furthermore, internal waves may introduce additional velocity variance to the near-glacier region, which should increase submarine melt rates.

Finally, the continual replacement of ambient fjord water with fresher recirculated plume water throughout the summer leads to a feedback cycle where LeConte Bay progressively freshens throughout the summer, while pycnoclines strengthen (Figures 3 and 4). As a result, gravity currents and along-fjord water velocities may also accelerate until subglacial discharge diminishes in the fall, or until a steady-state is reached. If 21st century projections of extreme warming in Alaska and western North America are realized (Christensen et al., 2013), then we anticipate the initiation of this feedback cycle will occur sooner in the spring and its cessation later in the fall. This transformation will expedite heat transport to LeConte Glacier for a greater portion of the year, which may independently become exaggerated due to warmer ocean temperatures and higher subaerial melt rates. Even in the absence of climate change, such a feedback cycle may also result from ice dynamics processes, such as a retreat along a retrograde slope, which would enhance subglacial discharge (Amundson & Carroll, 2018) and thus reflux.

Although heat advection is at a maximum in the summer, current ocean forcing parameterizations in ice sheet models would still likely overestimate heat advection to LeConte Glacier, due to the neglect of sill-driven mixing. In LeConte Bay, external shelf water accounts for less than half of the inflowing volume transport, and water temperatures near the glacier terminus are at least 3–4°C cooler than Frederick Sound surface water in the summer (Figure 4). This leads to the conflicting outcome that sill-driven mixing creates a circulatory cell that amplifies heat advection to the grounding line, yet the reflux of cold plume water simultaneously cools external water as it enters the fjord. Thus, the extrapolation of external water properties from sill depth to the grounding line, as done in the Ice Sheet Model Intercomparison Project for CMIP6 (Slater et al., 2020) and elsewhere (e.g., Khazendar et al., 2019), would greatly exaggerate near-glacier temperatures in LeConte Bay. Sill-driven mixing is, therefore, an under-appreciated component of fjord parameterizations, and its neglect may produce unreliable results in fjords with significant mixing.

### 4.3. Application to Other Glacial Fjords

Variability in subglacial discharge (Jackson & Straneo, 2016; Straneo et al., 2011), wind forcing (Jackson & Straneo, 2016; Jackson et al., 2014; Moffat, 2014; Moffat et al., 2018), and baroclinic exchange with the shelf (Carroll et al., 2018; Mortensen et al., 2011) have previously been observed as drivers of seasonal modes in glacial fjords. Our results indicate sill-driven mixing of glacial freshwater can also cause pronounced seasonal differences in stratification and circulation, particularly when coupled with subglacial discharge. When ambient fjord water is entrained and displaced by the subglacial discharge plume, mixing and reflux of freshwater at sills ensures it is replaced by fresher water. If this process continues for long enough, the entire water column above the grounding line, or above any obstructing secondary sills, will freshen adequately so that external water is quickly drawn from sill depth along pycnoclines directly to the glacier grounding line, provided it is located deeper than the sill (Carroll et al., 2017).

Despite the strong tidal forcing and shallow-silled geometry of LeConte Bay, the coupling of sill-generated mixing and plume-driven buoyancy forcing is not unique, and has been observed at other glacial fjords. Analogous seasonal behavior to LeConte Bay has been documented at Glacier Bay, Alaska (Matthews, 1981), Jorge Montt Fjord, Patagonia (Moffat et al., 2018), and Godthåbsfjord, Greenland (Mortensen et al., 2014, 2013). At these fjords, summer stratification routes warm surface water along a series of sills and pycnoclines to reach glacier termini at depth. In all cases, the summer regime was associated with the downward mixing of freshwater at entrance sills, leading to a ≲10% increase in subsurface freshwater fractions at Godthåbsfjord and Jorge

Montt Fjords between winter and summer (Matthews, 1981; Moffat et al., 2018; Mortensen et al., 2013). Similar seasonality and associated freshwater mixing have also been observed at other shallow-silled fjords throughout Southeast Alaska (Muench & Heggie, 1978; Walters et al., 1988), and may be an important control on heat transport to tidewater glaciers throughout that region.

MITgcm modeling of Ilulissat Icefjord, Greenland, suggests the reflux of glacial freshwater can occur even in instances where a subsurface outflowing plume intersects a sill at depth (Gladish et al., 2015). In their experiment, Gladish et al. (2015) showed that the subglacial discharge plume from Jakobshavn Glacier may reach neutral buoyancy at a similar depth to the 245 m entrance sill. The resultant subsurface outflowing plume mixed with inflowing external water at the entrance sill, resulting in cooler fjord water than other scenarios without subglacial discharge. Consistent with our flushing time estimates, fjord residence time increased in their model with additional subglacial discharge, and thus, presumably, the reflux of outflowing water at the sill. Residence time halved with the artificial deepening of the entrance sill by 450 m and the subsequent removal of the mixing zone. A similar process could also occur at Rink Isbrae, where the subsurface plume may intersect a 410 m deep sill at low subglacial discharge (Bartholomaus et al., 2016; Carroll et al., 2016).

Finally, the annual flux of iceberg meltwater often exceeds glacier-derived freshwater sources in glacial fjords, particularly when subglacial discharge is no longer at its maximum (Enderlin et al., 2016; Moon et al., 2018). As most of this meltwater remains at depth (Moon et al., 2018), it seems probable that iceberg meltwater will affect reflux in many silled fjords, particularly in locations where sills ground large icebergs at mixing zones (e.g., Sulak et al., 2017).

## 5. Conclusions

Through pairing extensive observations with three-dimensional numerical modeling, we demonstrated that the reflux of glacial freshwater at fjord sills can lead to distinct seasonal circulation regimes, particularly when paired with plume-driven buoyancy forcing. At LeConte Bay, the majority of glacial freshwater is refluxed at the shallow entrance sill during the summer, which together with subglacial plume entrainment, readily freshens all fjord water above the grounding line or secondary sills. The resultant stratification enables warm water to flow from the surface of Frederick Sound directly to the LeConte Glacier grounding line at 200 m depth, 25 km from the entrance sill. We expect this summertime circulation to enhance frontal ablation through increasing heat advection to the glacier terminus and forming internal tides; however, further work is needed to quantify the relationship between reflux and near-glacier water properties, and whether this has a significant affect on glacier dynamics.

Similar seasonal circulation regimes to LeConte Bay have been observed at glacial fjords in Patagonia, Greenland, and Alaska, and thus we anticipate our findings to be applicable across many settings. Although LeConte Bay behaves as a relatively simple fjord where shelf exchange only occurs through tidal forcing, similar seasonal patterns have been observed in other fjords of varying geometries. This suggests that freshwater reflux is an important control on circulation and heat advection in many glacial fjords, and is likely to be a critical component to any box-model fjord parameterization.

## Data Availability Statement

All observational data has been archived with the NOAA National Centers for Environmental Information at https://www.ncei.noaa.gov/archive/accession/0189574 (Sutherland et al., 2019b). The subglacial discharge model is archived with the Arctic Data Center at https://doi.org/10.18739/A22G44 (Amundson et al., 2017). All MITgcm model output and code for calculating TEF and efflux/reflux budgets are archived with Zenodo at https://doi.org/10.5281/zenodo.6377142 and https://doi.org/10.5281/zenodo.6377200 (Hager et al., 2022a, 2022b).

## References

Amundson, J. M., & Carroll, D. (2018). Effect of topography on subglacial discharge and submarine melting during tidewater glacier retreat. *Journal of Geophysical Research: Earth Surface*, *123*(1), 66–79. https://doi.org/10.1002/2017JF004376

Amundson, J. M., Kienholz, C., Hager, A. O., Jackson, R. H., Motyka, R. J., Nash, J. D., & Sutherland, D. A. (2020). Formation, flow and break-up of ephemeral ice mélange at LeConte Glacier and Bay, Alaska. *Journal of Glaciology*, *66*, 577–590. https://doi.org/10.1017/jog.2020.29

Amundson, J. M., Kienholz, C., Motyka, R., Sutherland, D., & Nash, J. (2017). Collaborative Research: Impact of subglacial discharge on turbulent plume dynamics and ocean-glacier heat and mass transfer, Southeast Alaska, 2016–2017. [Dataset]. Arctic Data Center. https://doi.org/10.18739/A22G44

Bamber, J., Tedstone, A., King, M., Howat, I., Enderlin, E., Van Den Broeke, M., & Noel, B. (2018). Land ice freshwater budget of the Arctic and North Atlantic Oceans: 1. Data, methods, and results. *Journal of Geophysical Research: Oceans*, *123*(3), 1827–1837. https://doi.org/10.1002/2017JC013605

Bamber, J., Van Den Broeke, M., Ettema, J., Lenaerts, J., & Rignot, E. (2012). Recent large increases in freshwater fluxes from Greenland into the North Atlantic. *Geophysical Research Letters*, *39*(19). https://doi.org/10.1029/2012GL052552

Bartholomaus, T. C., Stearns, L. A., Sutherland, D. A., Shroyer, E. L., Nash, J. D., Walker, R. T., et al. (2016). Contrasts in the response of adjacent fjords and glaciers to ice-sheet surface melt in West Greenland. *Annals of Glaciology*, *57*(73), 25–38. https://doi.org/10.1017/aog.2016.19

Burchard, H., Bolding, K., Feistel, R., Gräwe, U., Klingbeil, K., MacCready, P., et al. (2018). The Knudsen theorem and the Total Exchange Flow analysis framework applied to the Baltic Sea. *Progress in Oceanography*, *165*, 268–286. https://doi.org/10.1016/j.pocean.2018.04.004

Carroll, D., Sutherland, D. A., Curry, B., Nash, J. D., Shroyer, E. L., Catania, G. A., et al. (2018). Subannual and seasonal variability of Atlantic-origin waters in two adjacent West Greenland fjords. *Journal of Geophysical Research: Oceans*, *123*, 6670–6687. https://doi.org/10.1029/2018JC014278

Carroll, D., Sutherland, D. A., Hudson, B., Moon, T., Catania, G. A., Shroyer, E. L., et al. (2016). The impact of glacier geometry on meltwater plume structure and submarine melt in Greenland fjords. *Geophysical Research Letters*, *43*(18), 9739–9748. https://doi.org/10.1002/2016GL070170

Carroll, D., Sutherland, D. A., Shroyer, E. L., Nash, J. D., Catania, G. A., & Stearns, L. A. (2015). Modeling turbulent subglacial meltwater plumes: Implications for fjord-scale buoyancy-driven circulation. *Journal of Physical Oceanography*, *45*, 2169–2185. https://doi.org/10.1175/JPO-D-15-0033.1

Carroll, D., Sutherland, D. A., Shroyer, E. L., Nash, J. D., Catania, G. A., & Stearns, L. A. (2017). Subglacial discharge-driven renewal of tidewater glacier fjords. *Journal of Geophysical Research: Oceans*, *122*, 6611–6629. https://doi.org/10.1002/2017JC012962

Christensen, J. H., Kanikicharla, K. K., Aldrian, E., An, S. I., Cavalcanti, I. F. A., de Castro, M., et al. (2013). Climate phenomena and their relevance for future regional climate change. In *Climate change 2013 the physical science basis: Working group I contribution to the Fifth Assessment Report of the Intergovernmental Panel on Climate Change* (pp. 1217–1308). Cambridge University Press. https://doi.org/10.1017/CBO9781107415324.028

Cokelet, E. D., & Stewart, R. J. (1985). The exchange of water in fjords: The efflux/reflux theory of advective reaches separated by mixing zones. *Journal of Geophysical Research*, *90*, 7287–7306. https://doi.org/10.1029/JC090iC04p07287

Cowton, T., Slater, D., Sole, A., Goldberg, D., & Nienow, P. (2015). Modeling the impact of glacial runoff on fjord circulation and submarine melt rate using a new subgrid-scale parameterization for glacial plumes. *Journal of Geophysical Research: Oceans*, *120*(2), 796–812. https://doi.org/10.1002/2014JC010324

Davison, B. J., Cowton, T. R., Cottier, F. R., & Sole, A. J. (2020). Iceberg melting substantially modifies oceanic heat flux towards a major Greenlandic tidewater glacier. *Nature Communications*, *11*, 5983. https://doi.org/10.1038/s41467-020-19805-7

Dieng, H.-B., Cazenave, A., Meyssignac, B., & Ablain, M. (2017). New estimate of the current rate of sea level rise from a sea level budget approach. *Geophysical Research Letters*, *44*(8), 3744–3751. https://doi.org/10.1002/2017GL073308

Ebbesmeyer, C. C., & Barnes, C. A. (1980). Control of a fjord basin's dynamics by tidal mixing in embracing sill zones. *Estuarine and Coastal Marine Science*, *11*(3), 311–330. https://doi.org/10.1016/S0302-3524(80)80086-7

Eidam, E. F., Sutherland, D. A., Duncan, D., Kienholz, C., Amundson, J. M., & Motyka, R. J. (2020). Morainal bank evolution and impact on terminus dynamics during a tidewater glacier stillstand. *Journal of Geophysical Research: Earth Surface*, *125*. https://doi.org/10.1029/2019JF005359

Enderlin, E. M., Hamilton, G. S., Straneo, F., & Sutherland, D. A. (2016). Iceberg meltwater fluxes dominate the freshwater budget in Greenland's iceberg-congested glacial fjords. *Geophysical Research Letters*, *43*, 11287–11294. https://doi.org/10.1002/2016GL070718

Farmer, D. M., & Freeland, H. J. (1983). The physical oceanography of fjords. *Progress in Oceanography*, *12*, 147–220. https://doi.org/10.1016/0079-6611(83)90004-6

Gade, H., & Edwards, A. (1980). Deep water renewal in fjords. In *Fjord oceanography* (pp. 453–489). Springer. https://doi.org/10.1007/978-1-4613-3105-6_43

Gardner, A. S., Moholdt, G., Cogley, J. G., Wouters, B., Arendt, A. A., Wahr, J., et al. (2013). A reconciled estimate of glacier contributions to sea level rise: 2003 to 2009. *Science*, *340*(6134), 852–857. https://doi.org/10.1126/science.1234532

Geyer, W., & Cannon, G. (1982). Sill processes related to deep water renewal in a fjord. *Journal of Geophysical Research*, *87*, 7985. https://doi.org/10.1029/jc087ic10p07985

Geyer, W., & Ralston, D. (2011). The dynamics of strongly stratified estuaries. *Treatise on estuarine and coastal science* (pp. 37–52). Elsevier. https://doi.org/10.1016/B978-0-12-374711-2.00206-0

Gillibrand, P. A., Turrell, W. R., & Elliott, A. J. (1995). Deep water renewal in the upper basin of Loch Sunart, a Scottish fjord. *Journal of Physical Oceanography*, *25*(6), 1488–1503. https://doi.org/10.1175/1520-0485(1995)025<1488:DWRITU>2.0.co;2

Gladish, C. V., Holland, D. M., Rosing-Asvid, A., Behrens, J. W., & Boje, J. (2015). Oceanic boundary conditions for Jakobshavn Glacier. Part I: Variability and renewal of ilulissat icefjord waters, 2001–2014. *Journal of Physical Oceanography*, *45*(1), 3–32. https://doi.org/10.1175/JPO-D-14-0044.1

Hager, A., Sutherland, D., Amundson, J., Jackson, R., Kienholz, C., Motyka, R., & Nash, J. (2022a). Model results for: "Subglacial discharge reflux and buoyancy forcing drive seasonality in a silled glacial fjord", Part 1. [Dataset]. Zenodo. https://doi.org/10.5281/zenodo.6377142

Hager, A., Sutherland, D., Amundson, J., Jackson, R., Kienholz, C., Motyka, R., & Nash, J. (2022b). Model results for: "Subglacial discharge reflux and buoyancy forcing drive seasonality in a silled glacial fjord", Part 2. [Dataset]. Zenodo. https://doi.org/10.5281/zenodo.6377200

Hock, R. (1999). A distributed temperature-index ice-and snowmelt including potential direct solar radiation. *Journal of Glaciology*, *45*, 101–111. https://doi.org/10.3189/S0022143000003087

Hock, R., & Noetzli, C. (1997). Areal melt and discharge modeling of Storglaciären, Sweden. *Annals of Glaciology*, *24*, 211–216. https://doi.org/10.3189/S0260305500012192

Holland, D. M., Thomas, R. H., De Young, B., Ribergaard, M. H., & Lyberth, B. (2008). Acceleration of Jakobshavn Isbræ triggered by warm subsurface ocean waters. *Nature Geoscience*, *1*(10), 659–664. https://doi.org/10.1038/ngeo316

Jackson, R. H., Nash, J. D., Kienholz, C., Sutherland, D. A., Amundson, J. M., Motyka, R. J., et al. (2020). Meltwater intrusions reveal mechanisms for rapid submarine melt at a tidewater glacier. *Geophysical Research Letters*, *47*, e2019GL085335. https://doi.org/10.1029/2019GL085335

Jackson, R. H., Shroyer, E. L., Nash, J. D., Sutherland, D. A., Carroll, D., Fried, M. J., et al. (2017). Near-glacier surveying of a subglacial discharge plume: Implications for plume parameterizations. *Geophysical Research Letters*, *44*, 6886–6894.

Jackson, R. H., & Straneo, F. (2016). Heat, salt, and freshwater budgets for a glacial fjord in Greenland. *Journal of Physical Oceanography*, *46*, 2735–2768. https://doi.org/10.1175/JPO-D-15-0134.1

Jackson, R. H., Straneo, F., & Sutherland, D. A. (2014). Externally forced fluctuations in ocean temperature at Greenland glaciers in non-summer months. *Nature Geoscience*, *7*(7), 503–508. https://doi.org/10.1038/NGEO2186

Jenkins, A. (2011). Convection-driven melting near the grounding lines of ice shelves and tidewater glaciers. *Journal of Physical Oceanography*, *41*, 2279–2294. https://doi.org/10.1175/JPO-D-11-03.1

Joughin, I., Alley, R. B., & Holland, D. M. (2012). Ice-sheet response to oceanic forcing. *Science*, *338*(6111), 1172–1176. https://doi.org/10.1126/science.1226481

Khazendar, A., Fenty, I. G., Carroll, D., Gardner, A., Lee, C. M., Fukumori, I., et al. (2019). Interruption of two decades of Jakobshavn Isbrae acceleration and thinning as regional ocean cools. *Nature Geoscience*, *12*(4), 277–283. https://doi.org/10.1038/s41561-019-0329-3

Kienholz, C., Amundson, J. M., Motyka, R. J., Jackson, R. H., Mickett, J. B., Sutherland, D. A., et al. (2019). Tracking icebergs with time-lapse photography and sparse optical flow, LeConte Bay, Alaska, 2016–2017. *Journal of Glaciology*, *65*, 195–211. https://doi.org/10.1017/jog.2018.105

Knudsen, M. (1900). Ein hydrographischer lehrsatz. *Annalen der Hydrographie und Maritimen Meteorologie*, *28*(7), 316–320.

Large, W. G., McWilliams, J. C., & Doney, S. C. (1994). Oceanic vertical mixing: A review and a model with a nonlocal boundary layer parameterization. *Reviews of Geophysics*, *32*(4), 363–403. https://doi.org/10.1029/94RG01872

Lorenz, M., Klingbeil, K., MacCready, P., & Burchard, H. (2019). Numerical issues of the Total Exchange Flow (TEF) analysis framework for quantifying estuarine circulation. *Ocean Science*, *15*, 601–614. https://doi.org/10.5194/os-15-601-2019

Luckman, A., Benn, D. I., Cottier, F., Bevan, S., Nilsen, F., & Inall, M. (2015). Calving rates at tidewater glaciers vary strongly with ocean temperature. *Nature Communications*, *6*(1), 1–7. https://doi.org/10.1038/ncomms9566

MacCready, P. (2011). Calculating estuarine exchange flow using isohaline coordinates. *Journal of Physical Oceanography*, *41*, 1116–1124. https://doi.org/10.1175/2011JPO4517.1

MacCready, P., Geyer, W. R., & Burchard, H. (2018). Estuarine exchange flow is related to mixing through the salinity variance budget. *Journal of Physical Oceanography*, *48*, 1375–1384. https://doi.org/10.1175/JPO-D-17-0266.1

MacCready, P., McCabe, R. M., Siedlecki, S. A., Lorenz, M., Giddings, S. N., Bos, J., et al. (2021). Estuarine circulation, mixing, and residence times in the Salish Sea. *Journal of Geophysical Research: Oceans*, *126*, e2020JC016738. https://doi.org/10.1029/2020JC016738

Magorrian, S. J., & Wells, A. J. (2016). Turbulent plumes from a glacier terminus melting in a stratified ocean. *Journal of Geophysical Research: Oceans*, *121*(7), 4670–4696. https://doi.org/10.1002/2015JC011160

Marshall, J., Adcroft, A., Hill, C., Perelman, L., & Heisey, C. (1997). A finite-volume, incompressible Navier Stokes model for studies of the ocean on parallel computers. *Journal of Geophysical Research C: Oceans*, *102*, 5753–5766. https://doi.org/10.1029/96JC02775

Matthews, J. (1981). The seasonal circulation of the Glacier Bay, Alaska fjord system. *Estuarine, Coastal, and Shelf Science*, *12*(6), 679–700. https://doi.org/10.1016/S0302-3524(81)80065-5

McNabb, R. W., Hock, R., & Huss, M. (2015). Variations in Alaska tidewater glacier frontal ablation, 1985–2013. *Journal of Geophysical Research: Earth Surface*, *120*(1), 120–136. https://doi.org/10.1002/2014JF003276

Moffat, C. (2014). Wind-driven modulation of warm water supply to a proglacial fjord, Jorge Montt Glacier, Patagonia. *Geophysical Research Letters*, *41*(11), 3943–3950. https://doi.org/10.1002/2014GL060071

Moffat, C., Tapia, F. J., Nittrouer, C. A., Hallet, B., Bown, F., Boldt Love, K., & Iturra, C. (2018). Seasonal evolution of ocean heat supply and freshwater discharge from a rapidly retreating tidewater glacier: Jorge Montt, Patagonia. *Journal of Geophysical Research: Oceans*, *123*(6), 4200–4223. https://doi.org/10.1002/2017JC013069

Moon, T., Sutherland, D. A., Carroll, D., Felikson, D., Kehrl, L., & Straneo, F. (2018). Subsurface iceberg melt key to Greenland fjord freshwater budget. *Nature Geoscience*, *11*, 49–54. https://doi.org/10.1038/s41561-017-0018-z

Mortensen, J., Bendtsen, J., Lennert, K., & Rysgaard, S. (2014). Seasonal variability of the circulation system in a West Greenland tidewater outlet glacier fjord, Godthåbsfjord (64°N). *Journal of Geophysical Research: Earth Surface*, *119*(12), 2591–2603. https://doi.org/10.1002/2014jf003267

Mortensen, J., Bendtsen, J., Motyka, R. J., Lennert, K., Truffer, M., Fahnestock, M., & Rysgaard, S. (2013). On the seasonal freshwater stratification in the proximity of fast-flowing tidewater outlet glaciers in a sub-arctic sill fjord. *Journal of Geophysical Research: Oceans*, *118*, 1382–1395. https://doi.org/10.1002/jgrc.20134

Mortensen, J., Lennert, K., Bendtsen, J., & Rysgaard, S. (2011). Heat sources for glacial melt in a sub-Arctic fjord (Godthåbsfjord) in contact with the Greenland ice sheet. *Journal of Geophysical Research: Oceans*, *116*. https://doi.org/10.1029/2010JC006528

Motyka, R. J., Dryer, W. P., Amundson, J., Truffer, M., & Fahnestock, M. (2013). Rapid submarine melting driven by subglacial discharge, LeConte Glacier, Alaska. *Geophysical Research Letters*, *40*, 5153–5158. https://doi.org/10.1002/grl.51011

Motyka, R. J., Hunter, L., Echelmeyer, K. A., & Connor, C. (2003). Submarine melting at the terminus of a temperate tidewater glacier, LeConte Glacier, Alaska, USA. *Annals of Glaciology*, *36*, 57–65. https://doi.org/10.3189/172756403781816374

Motyka, R. J., Truffer, M., Fahnestock, M., Mortensen, J., Rysgaard, S., & Howat, I. (2011). Submarine melting of the 1985 Jakobshavn Isbræ floating tongue and the triggering of the current retreat. *Journal of Geophysical Research: Earth Surface*, *116*(F1). https://doi.org/10.1029/2009JF001632

Muench, R., & Heggie, D. (1978). Deep water exchange in Alaskan subarctic fjords. In B. Kjerfve (Ed.), *Estuarine transport processes* (pp. 239–267).University of South Carolina Press.

Murray, T., Scharrer, K., James, T., Dye, S., Hanna, E., Booth, A., et al. (2010). Ocean regulation hypothesis for glacier dynamics in southeast Greenland and implications for ice sheet mass changes. *Journal of Geophysical Research: Earth Surface*, *115*(F3), F03026. https://doi.org/10.1029/2009JF001522

Nick, F. M., Vieli, A., Howat, I. M., & Joughin, I. (2009). Large-scale changes in Greenland outlet glacier dynamics triggered at the terminus. *Nature Geoscience*, *2*(2), 110–114. https://doi.org/10.1038/NGEO394

O'Neel, S., Echelmeyer, K., & Motyka, R. (2001). Short-term flow dynamics of a retreating tidewater glacier: LeConte Glacier, Alaska, USA. *Journal of Glaciology*, *47*(159), 567–578. https://doi.org/10.3189/172756501781831855

Sanford, L. P., Boicourt, W. C., & Rives, S. R. (1992). Model for estimating tidal flushing of small embayments. *Journal of Waterway, Port, Coastal, and Ocean Engineering*, *118*(6), 635–654. https://doi.org/10.1061/(ASCE)0733-950X(1992)118:6(635)

Schaffer, J., Kanzow, T., von Appen, W.-J., von Albedyll, L., Arndt, J. E., & Roberts, D. H. (2020). Bathymetry constrains ocean heat supply to Greenland's largest glacier tongue. *Nature Geoscience*, *13*(3), 227–231. https://doi.org/10.1038/s41561-019-0529-x

Sciascia, R., Straneo, F., Cenedese, C., & Heimbach, P. (2013). Seasonal variability of submarine melt rate and circulation in an East Greenland fjord. *Journal of Geophysical Research: Oceans*, *118*(5), 2492–2506. https://doi.org/10.1002/jgrc.20142

Slater, D. A., Felikson, D., Straneo, F., Goelzer, H., Little, C. M., Morlighem, M., et al. (2020). Twenty-first century ocean forcing of the Greenland ice sheet for modeling of sea level contribution. *The Cryosphere*, *14*, 985–1008. https://doi.org/10.5194/tc-14-985-2020

Slater, D. A., Straneo, F., Das, S., Richards, C., Wagner, T., & Nienow, P. (2018). Localized plumes drive front-wide ocean melting of a Greenlandic tidewater glacier. *Geophysical Research Letters*, *45*(22), 12–350. https://doi.org/10.1029/2018GL080763

Smagorinsky, J. (1963). General circulation experiments with the primitive equations: I. The basic experiment. *Monthly Weather Review*, *91*(3), 99–164. https://doi.org/10.1175/1520-0493(1963)091<0099:GCEWTP>2.3.CO;2

Smith, B., Fricker, H. A., Gardner, A. S., Medley, B., Nilsson, J., Paolo, F. S., et al. (2020). Pervasive ice sheet mass loss reflects competing ocean and atmosphere processes. *Science*, *368*(6496), 1239–1242. https://doi.org/10.1126/science.aaz5845

Stigebrandt, A. (1977). On the effect of barotropic current fluctuations on the two-layer transport capacity of a constriction. *Journal of Physical Oceanography*, *7*(1), 118–122. https://doi.org/10.1175/1520-0485(1977)007<0118:OTEOBC>2.0.CO;2

Stigebrandt, A. (1981). A mechanism governing the estuarine circulation in deep, strongly stratified fjords. *Estuarine, Coastal, and Shelf Science*, *13*(2), 197–211. https://doi.org/10.1016/S0302-3524(81)80076-X

Stommel, H., & Farmer, H. G. (1953). Control of salinity in an estuary by a transition. *Journal of Marine Research*, *12*(1), 13–20. https://doi.org/10.1357/002224021834614380

Straneo, F., & Cenedese, C. (2015). The dynamics of Greenland's glacial fjords and their role in climate. *Annual Review of Marine Science*, *7*, 89–112. https://doi.org/10.1146/annurev-marine-010213-135133

Straneo, F., Curry, R. G., Sutherland, D. A., Hamilton, G. S., Cenedese, C., Våge, K., & Stearns, L. A. (2011). Impact of fjord dynamics and glacial runoff on the circulation near Helheim Glacier. *Nature Geoscience*, *4*, 322–327. https://doi.org/10.1038/ngeo1109

Straneo, F., & Heimbach, P. (2013). North Atlantic warming and the retreat of Greenland's outlet glaciers. *Nature*, *504*(7478), 36–43. https://doi.org/10.1038/nature12854

Sulak, D. J., Sutherland, D. A., Enderlin, E. M., Stearns, L. A., & Hamilton, G. S. (2017). Iceberg properties and distributions in three Greenlandic fjords using satellite imagery. *Annals of Glaciology*, *58*, 92–106. https://doi.org/10.1017/aog.2017.5

Sutherland, D., Jackson, R. H., Kienholz, C., Amundson, J. M., Dryer, W., Duncan, D., et al. (2019a). Direct observations of submarine melt and subsurface geometry at a tidewater glacier. *Science*, *365*(6451), 369–374. https://doi.org/10.1126/science.aax3528

Sutherland, D., Jackson, R. H., Kienholz, C., Amundson, J. M., Dryer, W., Duncan, D., et al. (2019b). Water temperature, salinity, currents, and others collected by CTD and ADCP from MV Steller and MV Pelican in LeConte Bay, Alaska from 9 August 2016 to 18 September 2018 (NCEI Accession 0189574). [Dataset]. National Centers for Environmental Information. Retrieved from https://www.ncei.noaa.gov/archive/accession/0189574

Walters, R. A., Josberger, E. G., & Driedger, C. L. (1988). Columbia Bay, Alaska: An "upside down" estuary. *Estuarine, Coastal, and Shelf Science*, *26*, 607–617. https://doi.org/10.1016/0272-7714(88)90037-6

Wood, M., Rignot, E., Fenty, I., Menemenlis, D., Millan, R., Morlighem, M., et al. (2018). Ocean-induced melt triggers glacier retreat in Northwest Greenland. *Geophysical Research Letters*, *45*(16), 8334–8342. https://doi.org/10.1029/2018GL078024

Xu, Y., Rignot, E., Menemenlis, D., & Koppes, M. (2012). Numerical experiments on subaqueous melting of Greenland tidewater glaciers in response to ocean warming and enhanced subglacial discharge. *Annals of Glaciology*, *53*(60), 229–234. https://doi.org/10.3189/2012AoG60A139

Zhao, K. X., Stewart, A. L., & McWilliams, J. C. (2021). Geometric constraints on glacial fjord-shelf exchange. *Journal of Physical Oceanography*, *51*(4), 1223–1246. https://doi.org/10.1175/JPO-D-20-0091.1